ORIGINAL PAPER



On the performance of domain decomposition methods for modeling heterogenous materials

Ming Yang¹ • Soheil Soghrati^{1,2}

Received: 24 May 2021 / Accepted: 22 August 2021 / Published online: 20 September 2021 © The Author(s), under exclusive licence to Springer-Verlag GmbH Germany, part of Springer Nature 2021

Abstract

In this manuscript, we review the performance of domain decomposition methods (DDMs), implemented as a black-box module integrated with a finite element solver, for modeling materials with complex microstructures. In particular, we study the accuracy and computational cost associated with using the non-overlapping and overlapping Schwarz methods, together with required adjustments for each method to avoid convergence issues. Compared to conventional applications such as fluid—solid interaction, the DDM simulation of the mechanical behavior of materials with complex heterostructures could be a challenging task due to high stress concentrations along subdomain edges intersecting with multiple material interfaces. For linear elastic problems, this could lead to high local errors along sub-domain boundaries and especially at subdomain vertices, which requires meticulous updating of boundary conditions (nodal forces and displacements) along these edges to alleviate the error. However, for nonlinear (elastoplastic) problems, we show that such microstructural features prohibit the convergence of the non-overlapping Schwarz method. The remedy to such convergence difficulties is to implement the overlapping Schwarz method, with a high overlap percentage between adjacent subdomains to achieve a reasonable computational cost.

Keywords Domain decomposition method · Finite element method · Schwarz method · Microstructure · Plasticity

1 Introduction

Many engineering problems are multiscale in nature, which often prohibits the use of a direct numerical simulation (DNS) approach for analyzing their physical behavior. There are numerous examples of such problems, including modeling biomaterials (e.g., bone) [1,2] and simulating the mechanical behavior of composite structures (e.g., carbon fiber reinforced polymer plates) [3]. The main challenge towards using the finite element method (FEM) for handling such massive DNS problems is the excessive number of degrees of freedom (DOFs) needed to discretize the domain. At best, this leads to an unfeasibly high computational cost that necessitates using significant parallel computing resources to perform the simulation. However, an exceedingly large number of DOFs could

cause the ill-conditioning of the system's stiffness matrix due to round-off errors [4] and therefore the inability to perform the simulation regardless of available computing resources. Further, in highly nonlinear problems (e.g., simulating a material failure using damage and cohesive-contact models), even a moderately large number of degrees of freedom could lead to convergence difficulties. This often necessitates the use of an explicit solver rather than an implicit approach to address these convergence issues, which would be more computationally demanding [5,6]. For massive problems, convergence issues would eventually resurface even with the use of an explicit solver due to the excessively small time increment needed at each load step.

Due to the challenges outlined above, numerical techniques such as homogenization-based upscaling [3,7,8] and multiscale methods [9,10] are often employed as an alternative to DNS for simulating the mechanical behavior of structures with an underlying complex microstructure. In homogenization-based methods, a microscopic representative volume element (RVE) of the material is analyzed to evaluate its effective properties. This RVE could be simulated subject to different boundary conditions (BCs) such as displacement, traction, or periodic BCs. While the latter is



Soheil Soghrati soghrati.1@osu.edu

Department of Mechanical and Aerospace Engineering, The Ohio State University, 201 West 19th Avenue, Columbus, OH USA

Department of Materials Science and Engineering, The Ohio State University, 201 W. 19th Avenue, Columbus, OH, USA

shown to be one of the best choices in terms of avoiding stress concentrations along RVE boundaries [11,12], none of these BCs are realistic and a source of error in predicting the domain response. Moreover, deriving a constitutive model to simulate the material behavior at the macroscale requires evaluating a homogenized stress-strain envelope, i.e., the material response subject to loadings in different directions. Besides the significant computational cost associated with this process, the resulting macroscopic constitutive model is often not reliable for simulating the domain response under multi-axial loading conditions.

One of the major limitations of homogenization-based methods is to accurately simulate the response of heterogenous domains with a significant variation of microstructure (e.g., functionally-graded materials) or defects with a much wider scattering compared to embedded heterogeneities. One of the challenges in such problems is that the required RVE size could violate a key requirement of performing homogenization-based simulation, i.e., the macroscopic stress in the RVE can no longer be assumed constant and has significant variations within the RVE. In such cases, multiple statistical volume elements (SVEs) corresponding to different macroscopic points of the structure must be analyzed and use resulting effective properties to derive parameters of a constitutive model corresponding to that specific points. Besides being highly computationally demanding, as shown in [13], the selected SVE size for evaluating homogenized properties in this upscaling approach could have a huge impact on the macroscopic response (e.g., simulated damage pattern). In this approach, using a large SVE overlooks the scattering in microscopic material properties while reducing the SVE size could lead to unrealistic stress concentrations along their boundaries that adversely affect resulting homogenized properties.

Multiscale methods, which are often categorized as semiconcurrent and concurrent methods [14-16], can be used as an alternative to homogenization-based techniques to improve the accuracy. In a semi-concurrent method, different scales are solved separately and linked together via a data passing mechanism up and down the scales [12]. In concurrent methods (e.g., the FE² multiscale method [17]), different scales co-exist in an integrated model and continuously communicate with one another during the simulation [18]. However, some of the challenges encountered during a homogenization-based analysis still exist when in multiscale methods, as one must simulate the mechanical response of several SVEs at the microscale. For example, in the FE² method, an SVE is assigned to each quadrature point of elements discretizing the macroscopic domain and its mechanical behavior is simulated subject to a macroscopic strain to evaluate homogenized stresses [19]. While concurrent multiscale methods yield better accuracy than homogenization-based techniques, this comes at the cost of a significantly higher computational cost. Reduced order-modeling techniques, such as Transformation Field Analysis [20], Nonuniform Transformation Field Analysis [21], Proper Orthogonal Decomposition [22], and Self-consistent Clustering Analysis [23,24] can be implemented to reduce this computational burden. However, note that not every massive problem (e.g., a car crash test) can be simulated using a multiscale approach, which limits the application range of such methods. Therefore, in problems such as crash test simulations, a combination of over-simplifying the domain geometry and using homogenization-based methods is often employed to enable approximating the nonlinear response of the problem.

An alternative to either DNS or multiscale analyses, especially when the nature of the problem does not allow using the latter, is to implement mathematical decompositions classified into three classes: operator splitting, function-space decomposition, and domain decomposition. Compared to the first two techniques that are widely used in parallel computing [25], the domain decomposition method (DDM) ensures that independent computations are presented in each processor and data is only exchanged along with subdomain interfaces or small overlaps between subdomains [26]. The Schwarz alternating algorithm for the discretization of partial differential equations was the first DDM introduced in 1869. This method has shown a robust performance for solving both linear or nonlinear systems of equations [27] and has become one of the main techniques of choice for high-performance computational applications [28].

The domain partitioning (sub-structuring) feature also makes DDMs an attractive class of numerical techniques for parallel computing [29], which is essential for simulating complex physical phenomena [26]. These methods can be categorized into two main groups, namely the overlapping and non-overlapping DDMs. With a simple algorithmic structure and without special interface treatment between neighboring subdomains [29], overlapping DDMs were first introduced in the form of mathematical models [29-31] and gradually implemented into computational mechanics due to their easy implementation and high accuracy [32,33]. With the increase of computational power in the past few decades, non-overlapping DDMs have been fully developed and integrated with numerical techniques such as FEM, boundary element method (BEM), and the finite difference method (FDM) [32,34-36].

The finite element tearing and interconnecting (FETI) [37] and the balancing domain decomposition (BDD) [38] are two classes of non-overlapping DDMs introduced in the 1990s, which have successfully been applied to a variety of problems. In the FETI algorithm, the primary field is first approximated on non-overlapping subdomains and then continuity conditions along their interfaces are enforced using Lagrange multipliers [39]. The BDD method adds a coarse



problem to the Neumann-Neumann method for the iterative solution of the FE domain [40]. More recently, several modified techniques aiming at resolving implementation issues in FETI and BDD methods have been introduced, among which we can mention FETI-1, FETI-DP (Dual-Primal) [41–44], BDDC (BDD by Constraint) [45,46], and the corresponding nonlinear versions [47,48]. It is worth mentioning that the growth of parallel computing capabilities also benefits the application of DDMs by utilizing multi-core CPU and GPU hardware resources [25,49]. For example, a new class of methods named non-intrusive (or non-invasive) global-local coupling [50,51] is proposed, which shares several similarities with DDMs [52].

In this work, we study the performance of overlapping and non-overlapping Schwarz DDM for simulating the linear elastic and elastoplastic responses of materials with complex microstructures. These methods are chosen versus more advanced DDMs such as FETI/BDD, as the goal is to establish a black-box DDM solver capable of integrating with any commercial FE software, allowing only the use of nodal forces and displacements along each subdomain boundaries as input/output parameters. For the non-overlapping DDM, the main implementation challenges are associated with the underlying complex material microstructure, causing sub-domain boundaries intersecting with multiple material interfaces (e.g., embedded heterogeneities). Unlike typical non-overlapping Schwarz method applications such as fluid-solid interaction problems that often involve only two sub-domains, this results in high stress concentrations along multiple sub-domain boundaries used for partitioning the domain, which could significantly slow down or even prohibit convergence. We study these challenges, as well as required considerations in the implementation of the non-overlapping Schwarz method to ensure convergence. However, we show that despite addressing all implementation issues, this method may still not be able to achieve convergence for simulating the elastoplastic response of materials with heterogenous microstructures. In such cases, it would be necessary to implement the overlapping Schwarz method to resolve convergence issues, although this comes at the price of a higher computational cost. We study the impact of the overlap percentage of subdomains on the performance and introduce techniques to reduce the computational cost associated with the implementation of this method.

The remainder of this manuscript is structured as follows. In Sect. 2, we briefly present the governing equations for linear elastic and elastoplastic problems studied in this work. The implementation issues and required considerations for enhancing the performance of non-overlapping and overlapping Schwarz methods for simulating the linear elastic response of multi-partitioned heterogenous domains are discussed in Sect. 3. Section 4 is dedicated to discussing implementation aspects of these DDMs for simu-

lating the elastoplastic behavior of heterogenous domains. Three numerical examples are then presented in Sect. 5 to further analyze the performance, as well as demonstrating the application of overlapping and non-overlapping DDMs for simulating massive problems with intricate microstructures. Final concluding remarks are presented in Sect. 6.

2 Problem formulation

2.1 Linear elasticity

Consider an open domain $\Omega \subset \mathbb{R}^2$ with outward unit normal vector \mathbf{n} on its boundary $\partial \Omega = \Gamma$, which is subdivided into two distinct regions $\Gamma = \Gamma_{\mathbf{u}} \cup \Gamma_{\mathbf{t}}$ corresponding to Dirichlet and Neumann boundary conditions, respectively. The governing equations for a linear elasticity problem defined in Ω can then be expressed as: Find the displacement field \mathbf{u} such that

$$\begin{cases} \nabla \cdot \boldsymbol{\sigma} + \mathbf{b} = \mathbf{0} & \text{in } \Omega \\ \boldsymbol{\sigma} = \mathbb{C} : \boldsymbol{\varepsilon} & \text{in } \Omega \\ \boldsymbol{\varepsilon} = \frac{1}{2} \left(\nabla \mathbf{u} + \nabla \mathbf{u}^T \right) & \text{in } \Omega \\ \mathbf{u} = \bar{\mathbf{u}} & \text{on } \Gamma_{\mathbf{u}} \\ \boldsymbol{\sigma} \cdot \mathbf{n} = \mathbf{t} & \text{on } \Gamma_{\mathbf{t}}, \end{cases}$$
(1)

where $\mathbf{b}:\Omega\to\mathbb{R}^2$ is the body force, $\bar{\mathbf{u}}:\Gamma_{\mathbf{u}}\to\mathbb{R}^2$ is the prescribed displacement, and $\mathbf{t}:\Gamma_{\mathbf{t}}\to\mathbb{R}^2$ is the traction vector. Furthermore, $\mathbb C$ is the fourth-order elasticity tensor relating the stress tensor $\boldsymbol{\sigma}$ and the strain tensor $\boldsymbol{\varepsilon}$ as

$$\sigma = \lambda \operatorname{tr}(\boldsymbol{\varepsilon})\mathbf{I} + 2\mu\boldsymbol{\varepsilon},\tag{2}$$

where λ and μ are the Lame's constants, **I** is the identity tensor, and tr(.) is the trace operator.

In order to write the weak form of (1), we first decompose the displacement field as $\mathbf{u} = \mathbf{u}_0 + \mathbf{u}_d$, where $\mathbf{u}_d|_{\Gamma_{\mathbf{u}}} = \bar{\mathbf{u}}$ and $\mathbf{u}_0 = \mathbf{u}_{01} \cup \mathbf{u}_{02} \cup ... \cup \mathbf{u}_{0m}$. The weak form is then expressed as:

Find
$$\mathbf{u}_{0i} \in \mathcal{V} := \{\mathbf{u}_{0i} : \bar{\Omega}_i \to \mathbb{R}^2, \ \mathbf{u}_0|_{\Gamma_D} = \mathbf{0}\}$$
 such that

$$\sum_{i=1}^{m} \int_{\Omega_{i}} \mathbf{L}(\mathbf{u}_{0i} + \mathbf{u}_{d}) \cdot \mathbb{C}_{i} \mathbf{L}^{T} \mathbf{v}^{T} d\Omega + \int_{\Omega} \mathbf{v} \mathbf{b} d\Omega + \int_{\Gamma_{\mathbf{t}}} \mathbf{w} \mathbf{t} d\Gamma = \mathbf{0} \ \forall \mathbf{v} \in \mathcal{V},$$
(3)

where the differential operator L is given by

$$\mathbf{L} = \begin{bmatrix} \frac{\partial}{\partial x} & 0 & \frac{\partial}{\partial x} \\ 0 & \frac{\partial}{\partial y} & \frac{\partial}{\partial y} \end{bmatrix}. \tag{4}$$

The Galerkin approximation of \mathbf{u}_h in (3) is evaluated by replacing \mathcal{V} and \mathcal{W} with proper finite dimensional spaces



 $\mathcal{V}^h \subset \mathcal{V}$ and $\mathcal{W}^h \subset \mathcal{W}$. In the context of the standard FEM, \mathcal{V}^h and \mathcal{W}^h are the space of Lagrangian shape functions used for approximating the field in each element.

2.2 Elastoplastic response

In order to write the governing equations for elastoplastic problems, we first define the deviatoric stress tensor s and strain tensor e as [53]

$$\begin{cases} s = \sigma - \frac{1}{3} \text{tr}(\sigma) \mathbf{I} \\ e = \varepsilon - \frac{1}{3} \text{tr}(\varepsilon) \mathbf{I}. \end{cases}$$
 (5)

For small strains in the plastic phase, the strain and stress tensors, as well as their rates, can be written as

$$\begin{cases} \boldsymbol{\varepsilon} = \boldsymbol{\varepsilon}^{e} + \boldsymbol{\varepsilon}^{p} \\ \dot{\boldsymbol{\varepsilon}} = \dot{\boldsymbol{\varepsilon}}^{e} + \dot{\boldsymbol{\varepsilon}}^{p} \\ \boldsymbol{\sigma} = \mathbb{C}_{i} : (\boldsymbol{\varepsilon} - \boldsymbol{\varepsilon}^{p}) \\ \dot{\boldsymbol{\sigma}} = \mathbb{C}_{i} : (\dot{\boldsymbol{\varepsilon}} - \dot{\boldsymbol{\varepsilon}}^{p}), \end{cases}$$

$$(6)$$

where superscript e and p denote elastic and plastic portions, respectively [54]. The von Mises yield criterion is used to determine the initiation of the nonlinear plastic behavior as [55]

$$f(\boldsymbol{\sigma}) = \sqrt{\frac{3}{2}\boldsymbol{s} : \boldsymbol{s}} - \sigma_{\mathbf{Y}} - H\boldsymbol{p} \le 0, \tag{7}$$

where σ_Y is the uniaxial strength, H is the isotropic hardening modulus, and p is the cumulated equivalent plastic strain. For a given elastic modulus E and the tangent elastic modulus E_t , H can be evaluated as

$$H = \frac{EE_t}{E - E_t}. (8)$$

In order to evaluate the path-dependent stress tensor during the FE simulation, an incremental analysis is utilized using an iterative predictor–corrector return mapping algorithm embedded in the Newton–Raphson global loop. This return mapping algorithm finds a new stress tensor σ_{n+1} and a plastic strain increment tensor Δp based on the stress tensor evaluated in the previous step σ_n , previous plastic strain p_n , and an increment of total deformation $\Delta \varepsilon$. Defining the elastic trial stress σ_t as

$$\sigma_t = \sigma_n + \mathbb{C}_i \Delta \varepsilon, \tag{9}$$

the plasticity criterion corresponding to σ_t is evaluated based on (7) as

$$\boldsymbol{f}_{t}(\boldsymbol{\sigma}_{t}) = \boldsymbol{\sigma}_{t}^{eq} - \sigma_{Y} - H \boldsymbol{p}_{n}, \tag{10}$$



where the equivalent stress tensor is given by

$$\sigma_t^{eq} = \sqrt{\frac{3}{2}s(\sigma_t) : s(\sigma_t)}.$$
 (11)

It is worth mentioning that in the Newton–Raphson solver, the tangent operator must be consistent with the time integration algorithm to achieve quadratic convergence [54,56]. The algorithmic consistent tangent matrix is given by

$$\mathbb{C}_{i}^{\text{tan}} = \mathbb{C}_{i} - 9\mu^{2} \left(\frac{1}{3\mu + H} - \frac{\Delta \mathbf{p}}{\sigma_{t}^{eq}} \right) \mathbf{n}_{s} \otimes \mathbf{n}_{s} - \frac{6\mu^{2}\Delta \mathbf{p}}{\sigma_{t}^{eq}} \mathbf{Dev}$$
(12)

where \mathbf{n}_s is the normal vector to the final yield surface given by $s\left(\sigma_t^{eq}\right)^{-1}$, \otimes is the standard tensor product, and **Dev** is the fourth-order tensor associated with the deviatoric operator [55].

3 DDM for linear elastic problems

The following five sub-sections focus on various implementation aspects of the non-overlapping Schwarz method for approximating the linear elastic response of heterogenous domains. Many of these implementation issues are shared with the overlapping Schwarz method, which are discussed in Sect. 3.6.

3.1 Domain partitioning and meshing

To facilitate describing the non-overlapping Schwarz method for multi-partitioned domains, the discussions presented next focus on a test problem with linear elastic behavior, a porous microstructure, and the boundary conditions shown in Fig. 1a. The displacement in the y direction is constrained along the bottom edge of this domain, while the bottom left corner is constrained in the x direction. Also, a uniform normal traction of $\bar{t}_v = 1 \text{ N m}^{-1}$ is applied along the top edge of the domain. The elastic modulus and Poisson's ratio of the material are $E = 50 \text{ N m}^{-2}$ and $\nu = 0.3$, respectively. As shown in Fig. 1b, the domain is subdivided into 16 nonoverlapping partitions in a 4×4 structured pattern. As noted previously, this manuscript aims at the implementation of DDMs as a black-box solver for modeling massive problems with complex microstructures, which requires subdividing the domain into multiple subdomains with a manageable size for a sequential solver. Because such domains could consist of thousands of embedded heterogeneities, regardless of the partitioning pattern, it would practically be impossible to avoid their intersections with subdomain boundaries.

Before discussing the implementation of the non-overlapping Schwartz method for modeling heterogenous domains, we

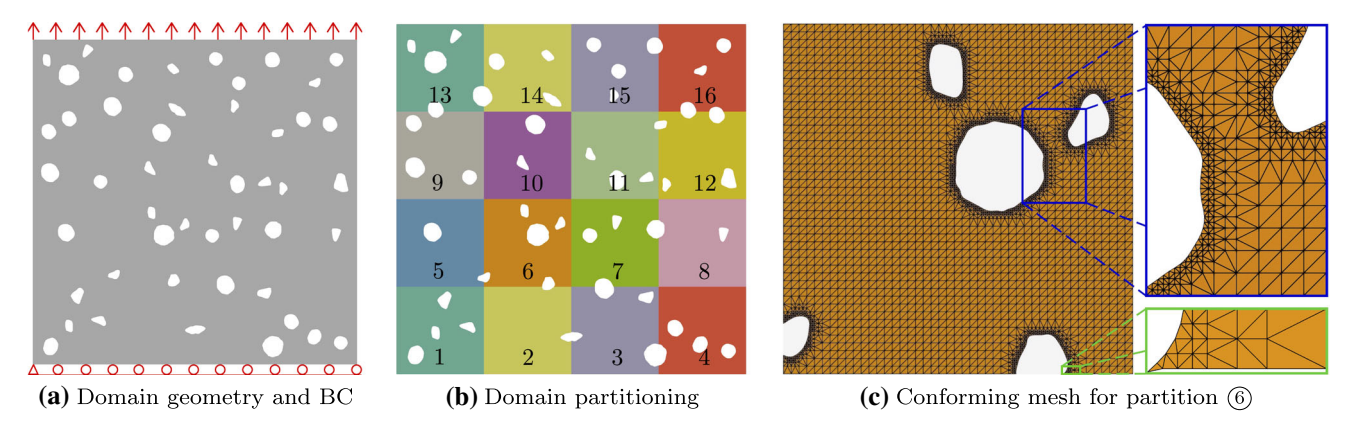


Fig. 1 Test problem used for describing the algorithm and implementation issues of the non-overlapping and overlapping Schwartz methods

must describe the FE mesh generation algorithm used for discretizing each subdomain. While in DDM the response of each subdomain is approximated independently subject to a set of boundary conditions (BCs) iteratively updated during the simulation, it may not be feasible to generate the FE model for each partition independently due to the complexity of microstructure. This is due to inevitable intersections between subdomain boundaries and embedded heterogeneities, which could form exceedingly sharp angles that result in elements with high aspect ratios. The presence of such elements in the mesh could be detrimental to predicting field gradients, which undermines the accuracy while updating BCs during a DDM simulation and could even prohibit convergence.

A more common strategy is to first generate a conforming mesh for the entire domain and then partition the mesh for a DDM simulation. While this approach can easily be employed for partitioning small domains such as the example problem shown in Fig. 1a, a parallel meshing algorithm is required to handle larger domains. For massive heterogenous domains, generating a conforming mesh in parallel for the entire domain could still be a computationally demanding task that might require massive parallel computing resources. Note that these challenges merely emerge from the complexity of the material microstructure, as there is no obligation to use meshes that conform across subdomain boundaries in the non-overlapping Schwartz method. Instead, techniques such as the nearest neighbor interpolation and weighted residual methods can be employed to update BCs at non-matching nodes [57], although minimizing the number of these nodes facilitates the implementation and enhances the convergence of DDM.

In this work, we implement the Conforming to Interface Structured Adaptive Mesh Refinement (CISAMR) algorithm introduced by Soghrati et al. [58,59] to create an FE model for each subdomain. CISAMR is a non-iterative meshing algorithm that transforms an initial (background) structured grid into a conforming mesh, ensuring that resulting ele-

ment aspect ratios do not exceed three for 2D problems. This process involves applying adaptive h-refinement, relocating mesh nodes (r-adaptivity), and subdividing elements. A unique feature of CISAMR is that only the nodes of background elements intersecting with material interfaces or domain boundaries are relocated during this transformation. Therefore, as far as background grids with the same element size are used for meshing all subdomains, only a handful of non-matching nodes might emerge along subdomain boundaries due to differences in local refinement levels in these regions. Figure 1c illustrates the conforming mesh generated using this algorithm for subdomain 6 of the test problem.

A key advantage of CISAMR for meshing a multipartitioned domain is the ability of this method to generate a conforming mesh for each subdomain independently, ensuring no degenerate element is formed along subdomain boundaries, while also minimizing the number of non-matching nodes across their interfaces. As shown in Fig. 2, this is simply achieved by using a slightly larger structured background grid for meshing each subdomain, extended by an additional layer of elements (coined *ghost* elements) in each direction. After creating the conforming mesh for each subdomain, we simply delete the ghost layer and any sub-elements generated within that during the CISAMR mesh transformation process. Therefore, this ghost layer serves as a buffer zone that avoids a sharp transition from fine to coarse elements across partition interfaces, which minimizes the number of non-matching nodes along with subdomain interfaces. More importantly, when an inclusion intersects a partition interfaces with an acute angle, this buffer zone automatically allows nodes to move away from the interface, which tapers this angle and avoids the formation of elements with high aspect ratios.

The lower inset of Fig. 1c shows that using CISAMR with a background mesh involving ghost elements allows the node on its bottom left corner to move away from the lower edge of ⑤ to form an element with a proper aspect ratio (< 3). This seemingly minuscule modification of the mesh structure is



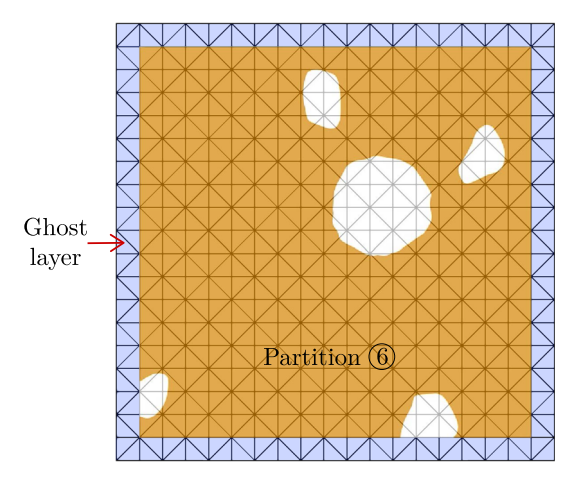


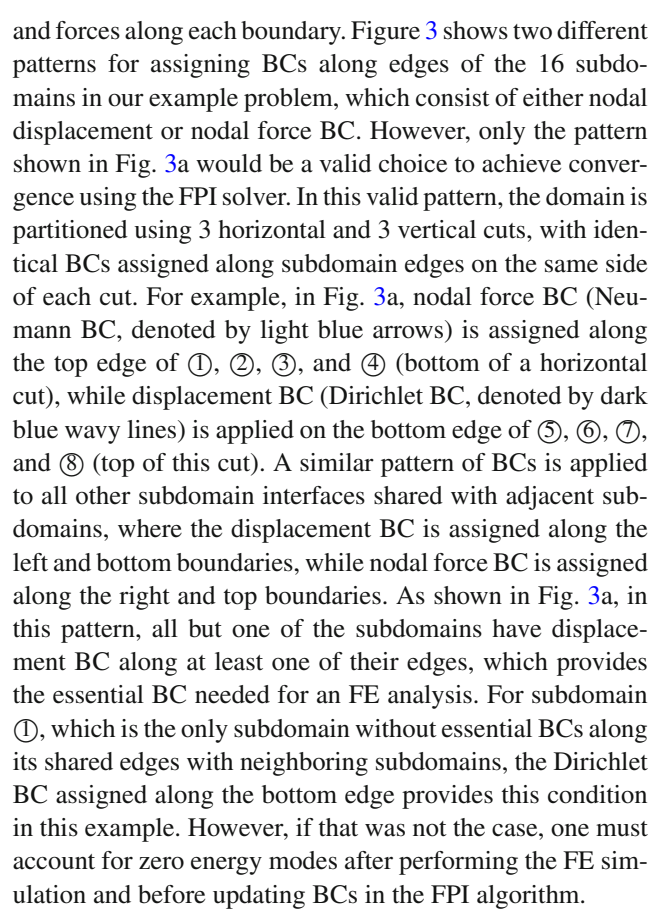
Fig. 2 Using a background mesh with a ghost layer of elements for meshing partition (6)

crucial to the performance of the DDM solver, as otherwise amplified gradient recovery errors at this point (which is a site of stress concentrations) could prohibit convergence. Also, note that using a ghost layer of elements in the background mesh for discretizing the adjacent subdomain (2) leads to an identical relocation of this node, resulting in matching nodes without any communication between these subdomains. Note that non-matching nodes can still emerge across subdomain interfaces in CISAMR meshes due to differences in adaptive refinement levels for nearby heterogeneities. It is worth mentioning that the idea of using ghost elements in CISAMR was originally introduced in [60] for the parallel implementation of this algorithm. However, given the fact that non-matching nodes along partition interfaces can easily be handled in the non-overlapping Schwarz method, here it is implemented sequentially to ensure the construction of high-quality meshes with no degenerate element in each subdomain.

It is worth noting that while the focus of this work is on modeling heterogenous materials, both CISAMR and the DDM techniques relying on this method can be applied to problems with arbitrary domain geometries and/or with non-rectangular subdomains [52,59]. However, additional considerations, such as an alternative domain partitioning approach, might be required to ensure the efficient approximation of the domain response in such cases.

3.2 Boundary conditions

After meshing each subdomain, appropriate Dirichlet and Neumann BCs must be assigned along their edges for a non-overlapping Schwarz simulation. As will be discussed in detail in Sect. 3.3, the fixed-point iteration (FPI) algorithm is employed to update subdomain BCs during the simulation by simultaneously enforcing the continuity of displacements



In the second pattern shown in Fig. 3b, force and displacement BCs are alternating at the corner of each subdomain, which results in assigning displacement (essential) BC along at least one edge of each subdomain. Although this pattern ensures all subdomains have sufficient essential BC for FE analysis, it is an inappropriate pattern for a DDM simulation due to the inability to update BCs at partition corners during the FPI process. For example, all subdomains have displacement BC at the corner point shared between ①, ②, ⑤, and ⑥, meaning the initial BC assigned to this point cannot be updated using the Dirichlet-to-Neumann approach described in Sect. 3.3, which prohibits the DDM convergence.

3.3 Iterative FPI solver

In order to perform a DDM simulation, we must first initialize BCs along with subdomain edges. The most straightforward approach is to initially assign zero displacements/forces to all subdomain boundary nodes, although a better initialization scheme will be introduced in Sect. 3.4. For the test problem shown in Fig. 1a, the sequential non-overlapping Schwarz simulation begins with approximating the field in subdomain ① subject to BCs shown in Fig. 3a, followed by using the FPI algorithm (described in the following paragraphs) to update BCs along adjacent subdomain edges, i.e., the left edge of ② and the bottom edge of ③. We then proceed to subdomain



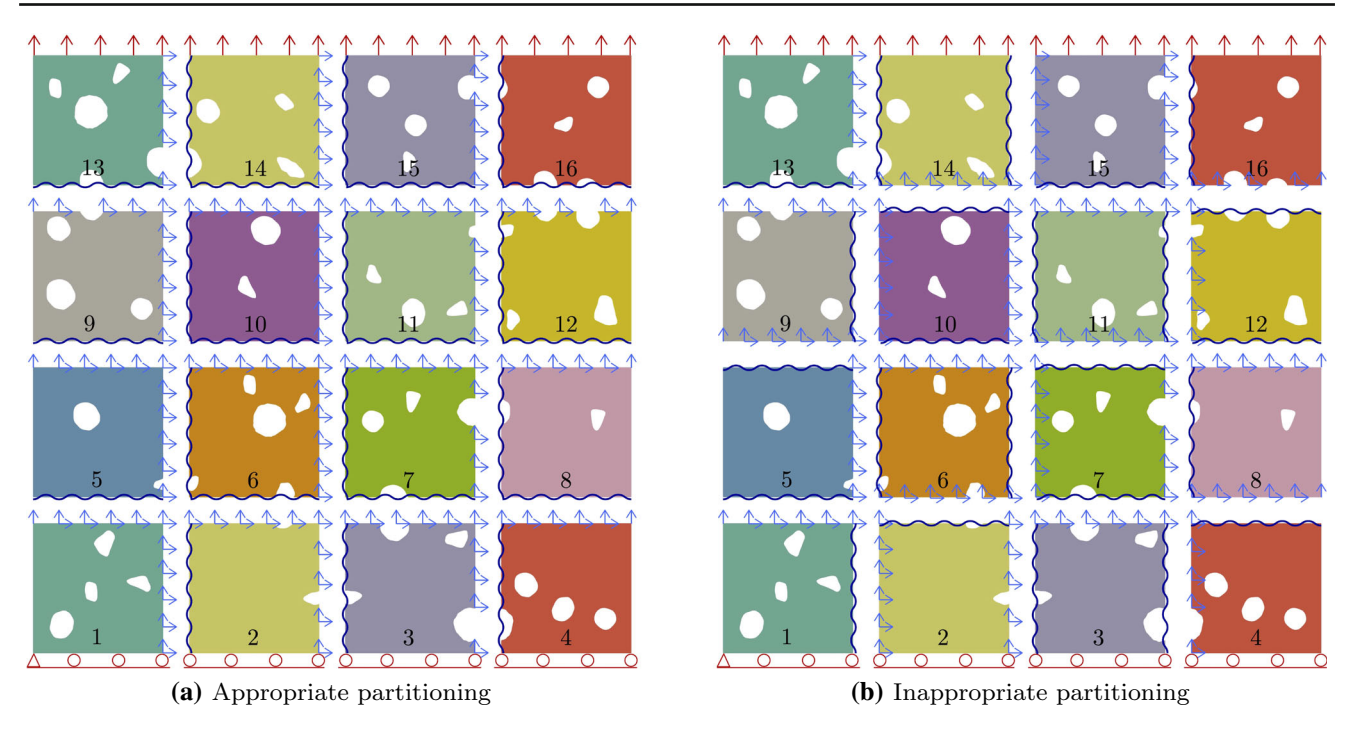


Fig. 3 Two different patterns for assigning BCs along subdomain edges in the non-overlapping Schwarz method, where wavy lines and arrows indicate nodal displacement and nodal force BCs, respectively

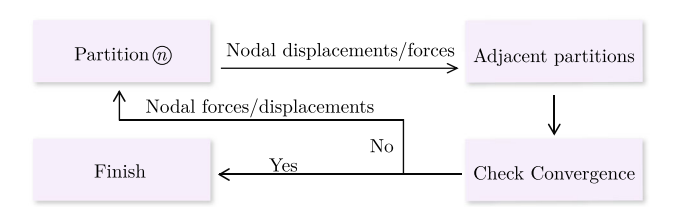


Fig. 4 FPI algorithm for updating nodal displacement and force BCs in a multi-partitioned domain

② and implement the same approach to update its adjacent subdomain BCs, which includes the right edge of ①. This process is recursively continued until all subdomains are visited and their neighboring subdomains BCs are updated (end of the first iteration). The iterations are then continued by restarting the process from subdomain ① until the continuity of forces and displacements are satisfied along with all subdomain interfaces within a given tolerance. Convergence criteria at iteration n+1 are given by

$$E_{\bar{\mathbf{u}}} = \frac{\|\bar{\mathbf{u}}_{n+1} - \bar{\mathbf{u}}_n\|}{\|\bar{\mathbf{u}}_n\|} < \text{tol}_{\bar{\mathbf{u}}},$$

$$E_{\mathbf{f}} = \frac{\|\mathbf{f}_{n+1} - \mathbf{f}_n\|}{\|\mathbf{f}_n\|} < \text{tol}_{\mathbf{f}},$$
(13)

where $\bar{\mathbf{u}}_n$ and \mathbf{f}_n are vectors of displacement and force BCs at all nodes along subdomain edges, while $\mathrm{tol}_{\bar{\mathbf{u}}}$ and $\mathrm{tol}_{\mathbf{f}}$ are tolerance values. The flowchart presented in Fig. 4 summarizes the algorithm discussed above.

Updating BCs using the FPI algorithm is a rather straightforward process, although special considerations are required for nodes at subdomain corners to ensure the DDM convergence. To facilitate the discussion, consider the interface between subdomains ① and ② in Fig. 3a. The nodal displacements $\bar{\mathbf{u}}_n^{\odot}$ recovered along the right edge of ① from the FE approximation of the field in this subdomain is used to update the displacement BC, $\bar{\mathbf{u}}_{n+1}^{\odot}$, along the left edge of ② as

$$\bar{\mathbf{u}}_{n+1}^{(2)} = \bar{\mathbf{u}}_n^{(1)}. \tag{14}$$

After approximating the field in ② using this updated displacement BC, the nodal forces $\mathbf{f}_{n+1}^{(1)}$ along the right edge of 1 are updated using an under-relaxation approach as

$$\mathbf{f}_{n+1}^{(1)} = (1 - \beta)\mathbf{f}_n^{(1)} - \beta\mathbf{f}_n^{(2)}, \tag{15}$$

where \mathbf{f}_n^{\odot} is the nodal force vector before the update, \mathbf{f}_n^{\odot} is the nodal force vector recovered along the left edge of \odot , and $\beta < 1$ is the relaxation factor. Note that β determines what portion of \mathbf{f}_n^{\odot} is used for updating nodal forces along the adjacent subdomain edge, which must be smaller than 1 to achieve convergence. In Sect. 3.5, we review some of the acceleration techniques used in DDM and examine their applicability for modeling heterogenous domains.

While FPI is a straightforward approach for enforcing continuity conditions along subdomain edges, there are a number



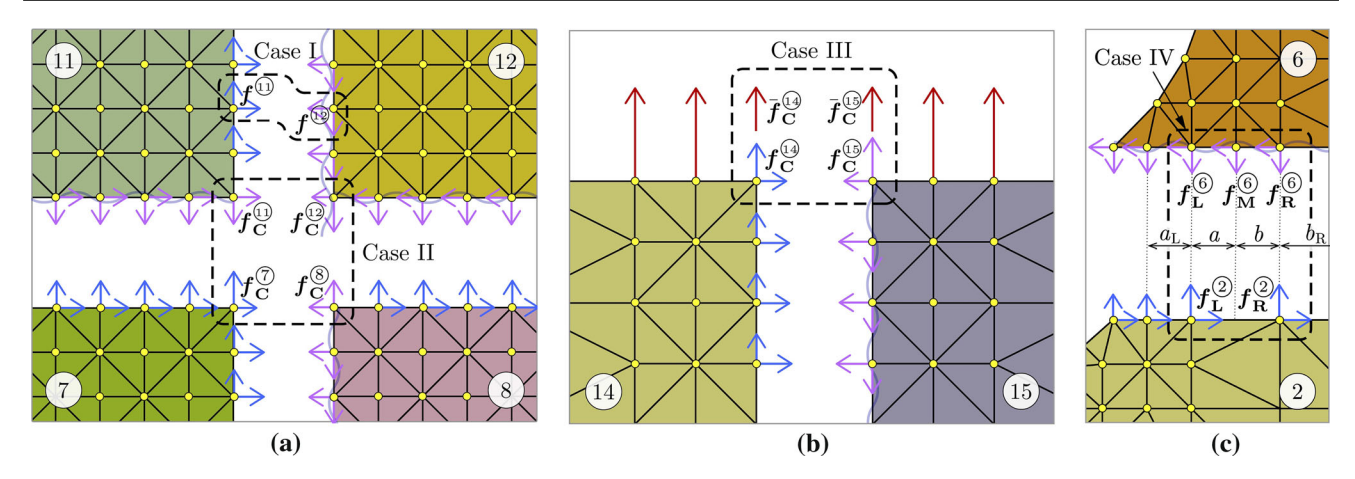


Fig. 5 Different case scenarios for updating nodal forces BCs (blue) along shared edges/corners of neighboring subdomain using nodal forces recovered from neighboring subdomain edges/corners (purple), where displacement BCs are applied. (Color figure online)

of important implementation aspects that are crucial to the convergence of this method for modeling multi-partitioned domains. Note that, unlike standard FEM, the inability to correctly update BCs even at a single node in this approach could prohibit convergence of the non-overlapping Schwarz method. In other words, the error does not remain local and pollutes the entire solution through FPI iterations. As shown in Fig. 5 and described in detail next, there are four different case scenarios that must be taken into account while updating nodal forces in a multi-partitioned domain that is discretized using the CISAMR algorithm. During the following discussion, the reader can also refer to Fig. 6, which shows nodal force values corresponding to each case in the test problem after the DDM approximation of its linear elastic response.

• Case I: The most common case scenario is updating the nodal force at a matching node on the interface (but not at a corner) shared between two adjacent subdomains. For example, consider the node highlighted at the interface between ① and ② in Fig. 5a, at which the continuity of nodal forces requires

$$f^{(1)} + f^{(2)} = 0. (16)$$

Using (15), the nodal force BC along the right edge of ① in the FPI process is updated as

$$f_{n+1}^{(\underline{0})} = (1-\beta)f_n^{(\underline{0})} - \beta f_n^{(\underline{0})}, \tag{17}$$

where $f_n^{\textcircled{1}}$ is the nodal force recovered at the left edge of 1 that has a displacement BC.

• Case II: Updating the force BC at the corner node of a subdomain (cf. Fig. 5a) requires simultaneously taking into account the contribution from all three neighboring subdomains. Based on the proposed pattern of assigning BCs along subdomain edges in Fig. 3a, only one of the four subdomains sharing each corner node has force BC along both its edges

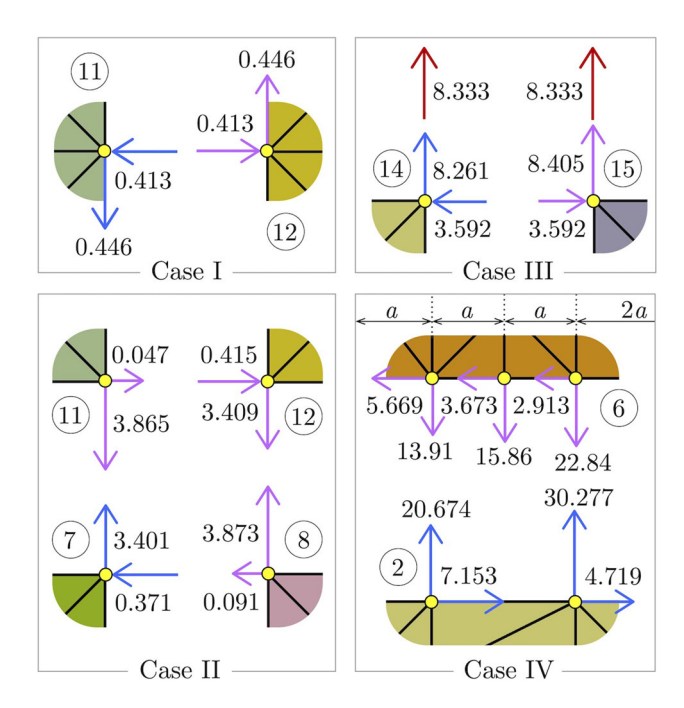


Fig. 6 Nodal force values at the nodes corresponding tor cases I–IV in Fig. 5 after the convergence of the non-overlapping Schwarz method

connected to this node, while the other three partitions have at least one edge with Dirichlet BC. For Case II in Fig. 5a, the top right corner node of ⑦ has nodal force BC, while ⑧, ①, and ② have displacement BC. Therefore, the displacement recovered at this node from ⑦ directly updates the displacement BC at corner nodes of the other three subdomains. To update the force BC at the top right corner of ⑦, we must simultaneously use nodal forces recovered at corner nodes of ⑧, ①, and ②, as the continuity condition at this node is given by

$$f_{\rm C}^{\bigcirc} + f_{\rm C}^{\circledcirc} + f_{\rm C}^{\bigcirc} + f_{\rm C}^{\bigcirc} = 0.$$
 (18)



Considering the relaxation effect, the nodal force BC at the corner node of (7) can then be updated as

$$f_{C_n+1}^{(7)} = (1-\beta)f_{C_n}^{(7)} - \beta(f_{C_n}^{(8)} + f_{C_n}^{(1)} + f_{C_n}^{(2)}).$$
 (19)

The inevitable presence of corner nodes in multi-partitioned domains could slow down the convergence of the nonoverlapping Schwarz method. This is due to the accumulation of error from multiple subdomains at such nodes while updating nodal force BCs. In some cases, resolving the convergence issue might necessitate using an exceedingly small β (e.g., $\beta = 0.05$), which could significantly increase the number of iterations and the overall computational cost. In extreme cases and especially in nonlinear problems, this could even prohibit convergence causing the fluctuation of error at corner nodes as the number of iterations increases. A similar issue is observed in other DDM techniques such as FETI, where special treatment of corner nodes (e.g., in FETI-DP) can significantly improve convergence. However, note that this manuscript aims to establish a black-box DDM framework that only utilizes nodal forces/displacements outputted by a commercial FE software, which does not allow access to the stiffness matrix of each subdomain to utilize more sophisticated techniques such as FETI-DP. Also, note that using an $N \times 1$ pattern for partitioning the domain to eliminate corner nodes would only be effective for a small number of subdomains. Our numerical studies show that for a large number of subdomains (N > 10), the high aspect ratio of subdomains and the corresponding errors associated with updating BCs at a large number of nodes along their interfaces in this pattern lead to severe convergence difficulties for the non-overlapping Schwarz method.

• Case III: This case scenario corresponds to corner nodes of two neighboring subdomains located on a domain boundary with Neumann (traction) BC, as shown in Fig. 5b. Here, $\bar{f}_C^{(3)}$ and $\bar{f}_C^{(3)}$ are external nodal forces at partition corners evaluated based on the traction \bar{t} applied along the upper edge of (4) and (5). During the FPI solution, we must update $f_C^{(4)}$, i.e., the nodal force on the top right corner of (4) based on the force recovered from the top left corner of (5). Satisfying the equilibrium condition at this node requires taking into account the presence of $\bar{f}_C^{(4)}$ and $\bar{f}_C^{(5)}$, which can be written as

$$f_{\rm C}^{(1)} + f_{\rm C}^{(1)} = \bar{f}_{\rm C}^{(4)} + \bar{f}_{\rm C}^{(5)}.$$
 (20)

The updated nodal force BC at the top right corner of (4) in the FPI solver can then be evaluated as

$$f_{\mathcal{C}_{n+1}}^{\bigcirc} = (1-\beta)f_{\mathcal{C}_n}^{\bigcirc} - \beta(f_{\mathcal{C}_n}^{\bigcirc} - \bar{f}_{\mathcal{C}}^{\bigcirc} - \bar{f}_{\mathcal{C}}^{\bigcirc}). \tag{21}$$

Note that effects of $\bar{f}_{\rm C}^{(4)}$ and $\bar{f}_{\rm C}^{(5)}$ have already been incorporated in evaluating the internal nodal force at this node

while approximating the FE response of each subdomain independently. However, it is essential to consider the sum of these external forces while updating the nodal force at the corner node located on this Neumann boundary, as internal forces $f_{\rm C}^{(3)}$ and $f_{\rm C}^{(3)}$ are not equal at this point. This statement is verified in Fig. 6 (Case III), which shows values of nodal forces after the convergence of DDM simulation.

• Case IV: As shown in Fig. 5c, the ghost elements used in the background mesh of CISAMR for creating the conforming mesh for each subdomain could lead to the presence of non-matching nodes along subdomain interfaces. Commonly used techniques in DDM simulations for the interpolation/projection of BCs between non-matching nodes include the nearest neighbor interpolation, interpolation by splines, and the Gauss interpolation technique [57]. However, when CISAMR meshes are generated using background meshes with the same element size for each subdomain, nonmatching nodes rarely emerge along partition interfaces and if so they are always located between two matching nodes. For example, see the middle node on the bottom edge of (6) (to be referred to as M[®]) in Fig. 5c, which does not match any node on the top edge of (2). The equilibrium of forces within the box shown in this figure requires that

$$f_{\rm L}^{(2)} + f_{\rm R}^{(2)} + f_{\rm L}^{(6)} + f_{\rm M}^{(6)} + f_{\rm R}^{(6)} = 0.$$
 (22)

Assume $M^{\textcircled{o}}$ has distances a and b from the matching nodes on its left and right on the bottom edge of o, i.e., nodes $L^{\textcircled{o}}$ and $R^{\textcircled{o}}$, respectively. Based on the equation above, nodal forces at $L^{\textcircled{o}}$ and $R^{\textcircled{o}}$ (left and right nodes on the top edge of o) are updated using the FPI algorithm as

$$f_{\mathcal{L}_{n+1}}^{\bigcirc} = (1-\beta)f_{\mathcal{L}_{n}}^{\bigcirc} - \beta \left(f_{\mathcal{L}_{n}}^{\bigodot} + \frac{b}{a+b}f_{\mathcal{M}_{n}}^{\bigodot}\right),$$

$$f_{\mathcal{R}_{n+1}}^{\bigcirc} = (1-\beta)f_{\mathcal{R}_{n}}^{\bigcirc} - \beta \left(f_{\mathcal{R}_{n}}^{\bigodot} + \frac{a}{a+b}f_{\mathcal{M}_{n}}^{\bigodot}\right).$$
(23)

After approximating the field in ②, the updated displacement BC at $M^{\textcircled{6}}$ is given by

$$\mathbf{u}_{\mathrm{M}}^{\textcircled{\textcircled{0}}} = \frac{b\mathbf{u}_{\mathrm{L}}^{\textcircled{\textcircled{2}}} + a\mathbf{u}_{\mathrm{R}}^{\textcircled{\textcircled{2}}}}{a+b}.\tag{24}$$

The BCs applied along subdomain edges in Fig. 5c could be reverse, meaning the displacement BC is assigned along the top edge of @ and the force BC is applied along the bottom edge of @. In this case, one must update nodal forces at $L^{@}$, $M^{@}$, and $R^{@}$ based on the forces recovered at $L^{@}$ and $R^{@}$. Note that the recovered force at $L^{@}$ corresponds to the effect of a (hypothetical) traction vector integrated along the length a_{L} to its left and and the length a + b to its right. Node $L^{@}$, at which we aim to update the force BC, also has the distance a_{L} from the node to its left. Given the continuity of tractions across the subdomains interface,



L[®] must receive the same portion of nodal force as L[®] from the traction applied to its right. However, node M[®] is at distance a from L[®], which is shorter than the distance a+b between L[®] and R[®]. Thus, node L[®] must receive $\frac{a}{a+b}$ times less force compared to L[®] from the traction on its right. Assuming a constant change of nodal forces between these two nodes (realistic assumption for a fine mesh), the relationship between nodal forces at L[®] and L[®] can then be written as

$$f_{\rm L}^{\textcircled{0}} = \frac{a_{\rm L} + a}{a_{\rm L} + a + b} f_{\rm L}^{\textcircled{2}}.$$
 (25)

Accordingly, the nodal forces at $L^{\textcircled{6}}$ and $R^{\textcircled{6}}$ following a similar reasoning are updated as

$$f_{\mathbf{L}_{n+1}}^{\bigodot} = (1-\beta) f_{\mathbf{L}_{n}}^{\bigodot} - \beta \frac{a_{\mathbf{L}} + a}{a_{\mathbf{L}} + a + b} f_{\mathbf{L}_{n}}^{\bigodot},$$

$$f_{\mathbf{R}_{n+1}}^{\bigodot} = (1-\beta) f_{\mathbf{R}_{n}}^{\bigodot} - \beta \frac{b_{\mathbf{R}} + b}{b_{\mathbf{R}} + a + b} f_{\mathbf{R}_{n}}^{\bigodot},$$
(26)

where b_R is the distance between $R^{\textcircled{2}}$ and the node to its right (cf. Fig. 5c).

Based on portions of nodal forces at $L^{\textcircled{2}}$ and $R^{\textcircled{2}}$ received by nodes $L^{\textcircled{6}}$ and $R^{\textcircled{6}}$, the equilibrium of forces given in (22) can be used to evaluate the updated nodal force at $M^{\textcircled{6}}$ as

$$f_{M_{n+1}}^{\bigodot} = (1-\beta)f_{M_n}^{\bigodot} - \beta \left(\frac{bf_{L_n}^{\bigodot}}{a_{L}+a+b} + \frac{af_{R_n}^{\bigodot}}{b_{R}+a+b}\right).$$
 (27)

However, using (27) to update the nodal force at $M^{\textcircled{\odot}}$ without paying attention to the requirement to satisfy the continuity of displacements across the interface between $L^{\textcircled{\odot}}$ and $R^{\textcircled{\odot}}$ leads to a high error in this region and prohibits the FPI convergence. Because $M^{\textcircled{\odot}}$ acts as a hanging node for the upper edge of $\textcircled{\odot}$, instead of applying a nodal force BC evaluated using (27), one must assign the following displacement BC at this node

$$\boldsymbol{u}_{\mathrm{M}}^{\textcircled{6}} = \frac{b\boldsymbol{u}_{\mathrm{L}}^{\textcircled{6}} + a\boldsymbol{u}_{\mathrm{R}}^{\textcircled{6}}}{a+b}.\tag{28}$$

It must be noted that mishandling a single hanging node in an FE approximation of the linear elastic response of a domain could only lead to local error in the vicinity of that node. However, the error associated with inaccurate updating of BC at a single hanging node on the subdomain edges could pollute the entire solution in a DDM simulation and even prohibit convergence. It is also worth mentioning that expanding (23)–(27) to cases with multiple non-matching nodes between $L^{\textcircled{2}}$ and $R^{\textcircled{2}}$ is rather straightforward, although detecting/handling such cases could considerably increase the implementation complexity. It is also worth mentioning while meshing each subdomain independently using CISAMR, the presence of non-matching nodes can easily

be avoided by applying a constant level of refinement along all subdomain edges similar to that applied along embedded heterogeneities.

3.4 Initialization of boundary conditions

As noted in Sect. 3.3, using the FPI algorithm to enforce continuity conditions along subdomain interfaces requires assigning initial force/displacement values to all boundary nodes to begin this iterative process. As noted previously, the most straightforward choice is to initialize nodal BCs as zero. For the test problem shown in Fig. 3a, this initialization approach leads to a zero field in subdomains (1)-(12) in the first iteration. Therefore, they do not contribute to updating BCs along shared edges with their neighboring subdomains at this iteration and a non-zero field is only approximated in subdomains (13)—(16) due to the traction BC applied along the top edge of the domain. However, even the resulting fields in these 4 subdomains are far from the exact solution due to unrealistic zero displacement BC or traction free BC applied along their other edges. Note that even after updating nodal force BCs along top edges of (9)–(12) based on the (inaccurate) fields approximated in (3)-(6), the fields approximated in the lower 8 subdomains still remains zero in the second iteration. In fact, the lowest 4 partitions only realize a small percentage of the traction BC applied on the top edge of the domain (due to the relaxation factor β used in the FPI algorithm) after 4 iterations. Figure 7a better shows the huge discrepancy between the initial and final fields that significantly increases the number of FPI iterations needed to achieve convergences.

To enhance the convergence of DDM for modeling multipartitioned heterogenous domains, subdomain BCs can be initialized based on the FE approximation of the field using a coarse mesh with effective material properties. The effective elastic modulus, $E_{\rm eff}$, for the porous domain of the test problem can be evaluated using the Mori-Tanaka homogenization approach as [61]

$$E_{\rm eff} = \frac{1 - V_{\rm p}}{1 + V_{\rm p}} E,\tag{29}$$

where $V_p=7.06\%$ is the volume fraction of pores. A coarse mesh (e.g., 10×10) can then be used to approximate the field in the homogenized domain. To initialize BCs of each subdomain for the DDM simulation, we first interpolate the nodal values for all nodes of each mesh from the initial field approximated using this coarse mesh. The resulting values on subdomain edges with displacement BC are then employed to initialize the BC along these edges. On edges with force BC, instead of initializing the nodal forces from the coarse mesh results, we directly evaluate nodal force values using the high-fidelity (fine) mesh created for that subdomain. In this approach, nodal values mapped from the coarse mesh



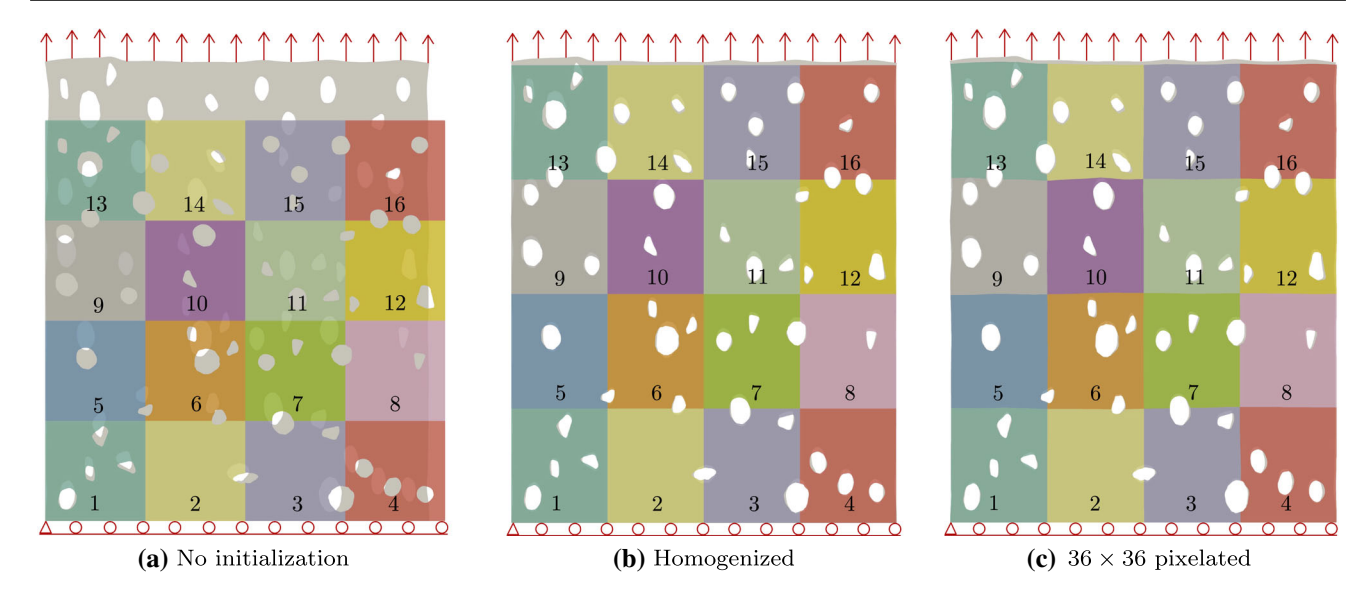


Fig. 7 Deformed shape of the test problems domain obtained from a DNS simulation versus $\bf a$ the undeformed domain corresponding to initializing subdomain BCs to zero; $\bf b$ deformed shape predicted using a coarse FE mesh with uniform effective properties; and $\bf c$ deformed

shape using a 36×36 pixelated mesh with effective properties calculated separately for each element. Deformed shapes are warped by a factor of 600

at nodes of elements adjacent to subdomain boundaries are used to recover the stress tensor in these elements. Using a nodal averaging scheme, these stresses are then employed to initialize nodal force BCs along these edges. Figure 7b compares the initial field approximated using this approach and the exact solution for the test problem, indicating a much better starting point for the FPI solver compared to using zero BCs to initialize the solution.

The accuracy of the initial field (and corresponding BCs) approximated on the coarse mesh can further be improved by calculating the effective property assigned to each element of this mesh separately. This will results in a *pixelated mesh*, that is particularly suited for modeling materials with a non-uniform spatial distribution of embedded heterogeneities. Figure 8 illustrates the variation of $E_{\rm eff}$ in a 36 \times 36 pixelated mesh generated using this approach for approximating the initial field for the test problem. A comparison between resulting initial and exact fields is depicted in Fig. 7c, which shows a small improvement compared to the case of using effective properties for the entire domain to approximate the initial field.

It is worth mentioning that due to difficulties associated with implementing the Mori-Tanaka approach for multi-material composites, we use the rule of mixtures to evaluate the effective properties needed for initializing BCs. For a bi-material composite, the effective elastic modulus can be evaluated as

$$E_{\text{eff}} = V^{I} E^{I} + (1 - V^{I}) E^{II}, \tag{30}$$

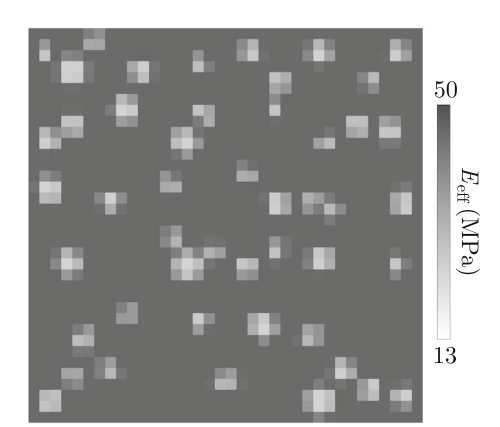


Fig. 8 36×36 pixelated mesh with varying homogenized elastic moduli in each element for the initialization of the DDM simulation

where E^I and E^{II} are the elastic moduli of each phase, while V^I and V^{II} are their volume fractions. Note that volume fractions of the composite constituents can easily be calculated using the high-fidelity meshes generated for the DDM simulation as

$$V^{I} = \frac{\Sigma A_{i}^{I}}{\Sigma A_{i}^{I} + \Sigma A_{j}^{II}},\tag{31}$$

where A_i^I and A_j^{II} are areas of conforming elements discretizing phase I and II, respectively.



3.5 Acceleration techniques and parallelization

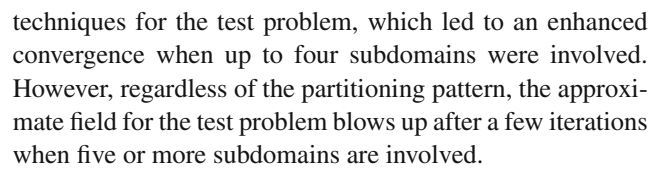
In order to accelerate the convergence of the non-overlapping Schwarz method, we studied a number of acceleration techniques to reduce the number of iterations compared to the FPI algorithm with a constant β . One of the well-known acceleration techniques is the Aitken's dynamic relaxation approach [62], where β is dynamically updated at each iteration as

$$\beta_{n+1} = \beta_n \frac{\mathbf{f}_{n-1}^{\top} (\mathbf{f}_n - \mathbf{f}_{n-1})}{(\mathbf{f}_n - \mathbf{f}_{n-1})^{\top} (\mathbf{f}_n - \mathbf{f}_{n-1})},$$
(32)

with \top denoting the transpose operator. In an FPI approximation with two subdomains (e.g., fluid-solid interaction problems), the Aitken's method can significantly enhance the convergence without imposing a notable computational overhead. However, as expected, our numerical studies showed that this acceleration technique fails to converge for modeling heterogenous domains partitioned into more than two subdomains.

The inability of the Aitken's method to achieve convergence for multi-partitioned domains is attributed to the inter-coupling between BCs of all subdomains, as this method only uses the force BC from the last iterations of two neighboring subdomains for evaluating β . For example, updating nodal forces on the right edge of (1) using the Aitken's method relies on nodal forces recovered along the left edge of (2) (cf. Fig. 3a). However, BCs on other edges of (2) are also simultaneously updated due to interaction with the other two neighboring subdomains, i.e., ③ and ⑥. This inter-coupling of BCs between subdomains makes it impossible to update BCs along each edge only based on the field approximated in one of its neighboring subdomains, as the resulting approximate field has already been affected by updated BCs along other edges of that subdomain. This intercoupling effect could be better by studying how force BCs are updated at subdomain corners using (19), where nodal forces recovered from three neighboring subdomains contribute to updating the nodal force BC of one subdomain. It is noteworthy that even a strip partitioning pattern does not lead to the convergence of the Aitken's method when more than three subdomains are involved.

Besides the Aitken's method, we studied the feasibility of using other acceleration techniques such as the vector extrapolation and quasi Newton schemes. Unlike the Aitken's method that only uses the results of the last iteration for approximating β , vector extrapolation methods try to find an approximate solution based on a converging vector series [63]. Several techniques can be employed to minimize the residuals of nodal forces or displacements, such as reduced rank extrapolation (RRE) [64] and minimal polynomial extrapolation (MPE) [65,66]. We tested both these



We also studied the feasibility of using the quasi-Newton method to accelerate the DDM simulation for multi-partition domains, which have proven to be robust and efficient for solving coupled fluid-solid interaction problems [67]. The interface quasi-Newton (IQN) solver was implemented, where an inverse Jacobian is extracted from force residuals and minimized using either the IQN least squares (IQNLS) or the IQN multiple vector Jacobian (IQNMVJ). The IQNLS algorithm is a matrix-free approach that yields an approximation of the inverse Jacobian of residuals, while the IQNMVJ algorithm stores the Jacobian matrix and implicitly estimates the inverse Jacobian using information from previous iterations [68]. Although both IQNLS and IQNMVJ have proven to significantly accelerate the DDM simulation for various coupled problems [69-71], as well as parallel implementation [72,73], our numerical results showed these methods fail to converge for multi-partitioned heterogenous domains. When only two partitions were used, IQN methods yielded a relatively similar convergence rate as the Aitken's and vector extrapolation methods. However, neither the IQNLS nor the IQNMVJ was capable of achieving convergence when more than four subdomains were used in the non-overlapping Schwarz method.

It is worth noting that techniques such as the Lagrange multipliers used in FETI or coarse problem for pre-conditioner in BDD can be regarded as acceleration methods that can successfully handle multi-partition domains. However, these methods are not considered in the current manuscript, as the goal is to establish a black-box DDM solver that only uses displacements and/or nodal forces along subdomain boundaries as input/output parameters.

3.6 Overlapping Schwarz method

In Sect. 5, we show that the non-overlapping Schwarz method could face severe convergence difficulties for modeling heterogenous domains with an elastoplastic material behavior. The overlapping Schwarz method can resolve this challenge and achieve convergence regardless of the complexity of the material microstructure. Figure 9 illustrates partitioning the test problem domain into 9 overlapping subdomains for such simulation. Note that in the overlapping Schwarz method, the percentage of overlap between adjacent subdomains is one of the key modeling parameters, with a higher percentage accelerating the convergence but simultaneously increasing the cost associated with the FE approximation of the field in each subdomain [74]. In Sect. 5.1.1, we study the impact of



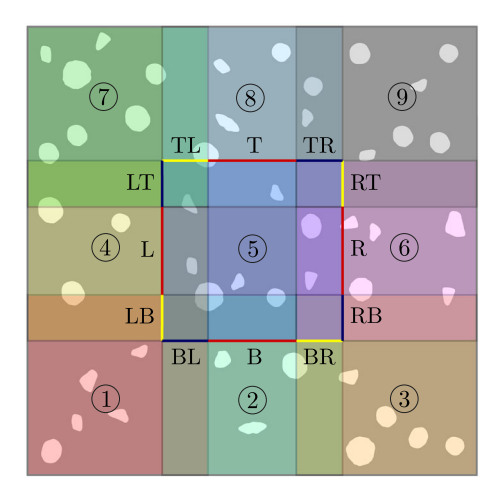


Fig. 9 Test problem domain subdivided into 9 overlapping subdomains, highlighting different portions of subdomain 3 edges based on how Dirichlet BCs are updated during an overlapping Schwarz simulation

this tradeoff on the overall computational cost for approximating the linear elastic response of the test problem.

In the overlapping Schwarz method, Dirichlet BCs are assigned along each subdomain edge and are iteratively updated based on the field approximated in their adjacent overlapping subdomains. Given that no nodal force recovery/updating is required in this approach, the implementation is more straightforward than the non-overlapping Schwarz method and intersections between subdomain edges and embedded heterogeneities no longer affect the performance. To describe the process of updating Dirichlet BCs in the overlapping Schwarz method, consider different partitions of subdomain ⑤ edges highlighted in Fig. 9. The Dirichlet BC in each segment is evaluated as the average of the FE approximation of the displacement in that location in adjacent overlapping subdomains, which can be written as

$$\begin{split} &\bar{\mathbf{u}}_{n+1}^{\mathrm{BL}^{\left(\bar{S}\right)}} = 0.5 \left(\bar{\mathbf{u}}_{n}^{\left(\bar{\Box}\right)} \right|_{\mathrm{BL}} + \bar{\mathbf{u}}_{n}^{\left(\bar{\Box}\right)} \right|_{\mathrm{BL}} \right), \quad \bar{\mathbf{u}}_{n+1}^{\mathrm{BS}^{\left(\bar{S}\right)}} = \bar{\mathbf{u}}_{n}^{\left(\bar{\Box}\right)} \right|_{\mathrm{B}}, \\ &\bar{\mathbf{u}}_{n+1}^{\mathrm{BR}^{\left(\bar{S}\right)}} = 0.5 \left(\bar{\mathbf{u}}_{n}^{\left(\bar{\Box}\right)} \right|_{\mathrm{BR}} + \bar{\mathbf{u}}_{n}^{\left(\bar{\Box}\right)} \right|_{\mathrm{BR}} \right), \quad \bar{\mathbf{u}}_{n+1}^{\mathrm{RS}^{\left(\bar{S}\right)}} = \bar{\mathbf{u}}_{n}^{\left(\bar{\Box}\right)} \right|_{\mathrm{R}}, \\ &\bar{\mathbf{u}}_{n+1}^{\mathrm{RT}^{\left(\bar{S}\right)}} = 0.5 \left(\bar{\mathbf{u}}_{n}^{\left(\bar{\Box}\right)} \right|_{\mathrm{RT}} + \bar{\mathbf{u}}_{n}^{\left(\bar{\Box}\right)} \right|_{\mathrm{RT}} \right), \\ &\bar{\mathbf{u}}_{n+1}^{\mathrm{TL}^{\left(\bar{S}\right)}} = 0.5 \left(\bar{\mathbf{u}}_{n}^{\left(\bar{\Box}\right)} \right|_{\mathrm{TL}} + \bar{\mathbf{u}}_{n}^{\left(\bar{\Box}\right)} \right|_{\mathrm{TL}} \right), \quad \bar{\mathbf{u}}_{n+1}^{\mathrm{TS}^{\left(\bar{S}\right)}} = \bar{\mathbf{u}}_{n}^{\left(\bar{S}\right)} \right|_{\mathrm{T}}, \\ &\bar{\mathbf{u}}_{n+1}^{\mathrm{TR}^{\left(\bar{S}\right)}} = 0.5 \left(\bar{\mathbf{u}}_{n}^{\left(\bar{\Box}\right)} \right|_{\mathrm{LR}} + \bar{\mathbf{u}}_{n}^{\left(\bar{\Box}\right)} \right|_{\mathrm{LB}} \right), \quad \bar{\mathbf{u}}_{n+1}^{\mathrm{LS}^{\left(\bar{S}\right)}} = \bar{\mathbf{u}}_{n}^{\left(\bar{\Box}\right)} \right|_{\mathrm{L}}, \\ &\bar{\mathbf{u}}_{n+1}^{\mathrm{LT}^{\left(\bar{S}\right)}} = 0.5 \left(\bar{\mathbf{u}}_{n}^{\left(\bar{\Box}\right)} \right|_{\mathrm{LT}} + \bar{\mathbf{u}}_{n}^{\left(\bar{\Box}\right)} \right|_{\mathrm{LT}} \right). \end{split}$$

Other implementation aspects of the overlapping Schwarz method for modeling heterogenous domains are similar to

those discussed previously for its non-overlapping counterpart. Using a structured pattern for partitioning the domain (cf. Fig. 9), the CISAMR algorithm is implemented to mesh each subdomain independently. Note that ghost elements are still employed in the background mesh to avoid the formation of high aspect ratio elements along subdomain edges during the meshing process. Also, Dirichlet BCs along subdomain edges are initiated based on an initial field approximated on a coarse pixelated mesh with effective properties for each element, as described in Sect. 3.4.

4 DDM for elastoplastic problems

Using either the overlapping or non-overlapping Schwarz method for simulating the nonlinear mechanical behavior of heterogenous domains requires addressing a number of additional implementation issues. As an example of nonlinear problems, in this work we focus on modeling the elastoplastic response of heterogenous materials, although the discussion provided next is general and can be used for simulating other nonlinear phenomena. Note that one of the main advantages of using DDM instead of DNS, even when the problem size might allow the latter, is enabling the use of an implicit solver for simulating the FE response of smaller subdomains. More than often, this is not the case for massive nonlinear FE problems, where the implicit solver may fail to converge and one must implement an explicit time integration scheme, resulting in a higher computational cost and in some cases a lower accuracy.

To begin an elastoplastic DDM simulation, we first break down the applied load into $N_{\rm load}$ steps (a similar approach can be used for displacement-controlled problems). $N_{\rm load}$ and the load increment can be selected adaptively based on the number of Newton–Raphson (NR) iterations needed for convergence at each step. Note that, at load step n, approximating the nonlinear response of each subdomain requires multiple load increments by the NR solver during the DDM simulation. In the following discussion, it is important to distinguish between the load increments and iterations needed for the DDM convergence for the entire domain and those of the nonlinear solver for each subdomain. To avoid confusion, we refer to the latter as local load step or iteration, while the term global will be used to refer to load steps and iterations for the DDM solver.

At the first global load step, the simulation is initialized similarly to a linear elastic problem, i.e., a pixelated mesh with homogenized elastic properties is employed to approximate the field $\mathbf{u}_1^{\text{init}}$ in the entire domain. Nodal displacement BCs, $\bar{\mathbf{u}}_1^{\text{init}}$, are then initialized using this field along subdomain interfaces with Dirichlet BC. In the non-overlapping Schwarz method, we also map $\mathbf{u}_1^{\text{init}}$ to the FE mesh generated for each subdomain to evaluate nodal forces $\mathbf{f}_1^{\text{init}}$ along



edges with force BC as

$$\mathbf{f}_{1}^{\text{init}} = -\int_{\Gamma_{\mathbf{f}}} \boldsymbol{\sigma}(\mathbf{u}_{1}^{\text{init}}) d\Gamma. \tag{34}$$

After the initialization of BCs, the iterative DDM simulation begins by using the Newton–Raphson solver to approximate the field in each subdomain, followed by updating force/displacement BCs along subdomain interfaces until continuity conditions are satisfied. Note that different numbers of local (Newton–Raphson) iterations might be required in each subdomain to approximate the field in each global (DDM) iteration.

Assume that the DDM simulation has reached the global load step n, where the displacement field and nodal force increments are given by $\Delta \mathbf{u}_n$ and $\Delta \mathbf{f}_n$, respectively. To approximate $\Delta \mathbf{u}_{n+1}$, we estimate the field in each subdomain for global load step n+1 to re-initialize nodal displacement increments at this step. Similar to the first load step, this initialization has a crucial impact on the number of global iterations (computational cost), where inappropriate initialization of BCs could even prohibit convergence. The most straightforward approach is to use the last converged displacement increment, $\Delta \mathbf{u}_n$, to re-initialize the field (and subsequently nodal BCs) as

$$\Delta \mathbf{u}_{n+1}^{\text{init}} = \Delta \mathbf{u}_n \frac{\|\Delta \bar{\mathbf{t}}_{n+1}\|}{\|\Delta \bar{\mathbf{t}}_n\|},\tag{35}$$

where $\Delta \bar{\mathbf{t}}_n$ is the global load increment at load step n. The nodal forces $\mathbf{f}_{n+1}^{\text{init}}$ corresponding to this initial displacement is calculated similarly to that of the first load step given in (34).

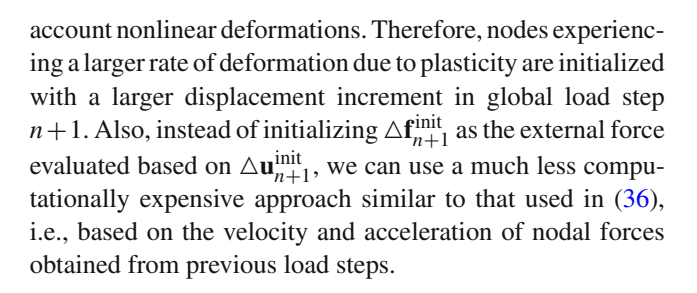
The initialization scheme above yields a reasonable estimate for $\mathbf{u}_{n+1}^{\text{init}}$ and $\mathbf{f}_{n+1}^{\text{init}}$, which can significantly reduce the number of global iterations compared to the case of zero BC initialization. However, we can further improve the initialization of nodal BCs by considering their rate of change due to nonlinear deformations. Note that initializing $\mathbf{u}_{n+1}^{\text{init}}$ using (35) relies on the assumption of linear deformation between global load steps n and n+1, which overlooks the nonlinear response of the material. Therefore, a better estimate for the initialization of $\mathbf{u}_{n+1}^{\text{init}}$ along edges with displacement BC can be written as

$$\Delta \bar{\mathbf{u}}_{n+1}^{\text{init}} = \bar{\mathbf{v}}_n \Delta \|\bar{\mathbf{t}}_{n+1}\| + \frac{\bar{\mathbf{v}}_n - \bar{\mathbf{v}}_{n-1}}{\Delta \bar{\mathbf{t}}_n} \|\Delta \bar{\mathbf{t}}_{n+1}\|^2, \tag{36}$$

where

$$\bar{\mathbf{v}}_n = \frac{\Delta \bar{\mathbf{u}}_n - \Delta \bar{\mathbf{u}}_{n-1}}{\Delta \|\bar{\mathbf{t}}_n\|}.$$
(37)

Note that the second term in (36) is the rate of change of displacement increment in previous load steps that takes into



5 Results and discussion

5.1 Test problem

Before modeling massive problems, it is worthwhile to study the impact of DDM parameters such as the number of subdomains and initialization scheme on the convergence and computational cost of overlapping and non-overlapping Schwarz simulations for the test problem (cf. Fig. 1a).

5.1.1 Linear elastic response

The material properties and BCs used for simulating the linear elastic response of the test problem were presented in Sect. 3.1. Figure 10a illustrates the non-overlapping Schwarz approximation of the stress field σ_{22} in this problem after 80 iterations using $\beta = 0.15$ and the 4 \times 4 partitioning pattern shown in Fig. 3a (total number of elements: 93,063). Note that no discontinuity is observed in the stress field across subdomain interfaces in this simulation. We have also compared this result with DNS of the field using a similar CISAMR mesh by l_2 norms of the errors associated with nodal displacements $||\mathbf{u}_{i}^{\text{DDM}} - \mathbf{u}_{i}^{\text{FEM}}||$ and nodal stresses $||\boldsymbol{\sigma}_{i}^{\text{DDM}} - \boldsymbol{\sigma}_{i}^{\text{FEM}}||$. Figure 10b, c illustrate the variation of these measures of the error in the test problem, indicating an excellent accuracy with no concentration of displacement error along subdomain interfaces. Although a small concentration of stress error is observed along subdomain edges, this is mainly due to a lack of nodal averaging during stress recovery in DDM results.

Figure 11 shows the variation of maximum nodal displacement and stress errors versus the number of DDM iterations for models with different subdomain numbers and initialization schemes ($\beta = 0.15$). For the 4 × 4 partitioning pattern studied previously, three simulations were conducted with (i) no initialization, (ii) initialized using the displacement field obtained from a homogeneous domain; and (iii) initialized using the field approximated on the 36 × 36 pixelated mesh shown in Fig. 8. Comparing these results clearly shows a slow convergence of the model with zero initialization of BCs. We also simulated non-overlapping Schwarz responses of two more models subdivided into 2 × 2 and 6 × 6 subdomains using $\beta = 0.2$ and 0.15, respectively (initialized using an FE



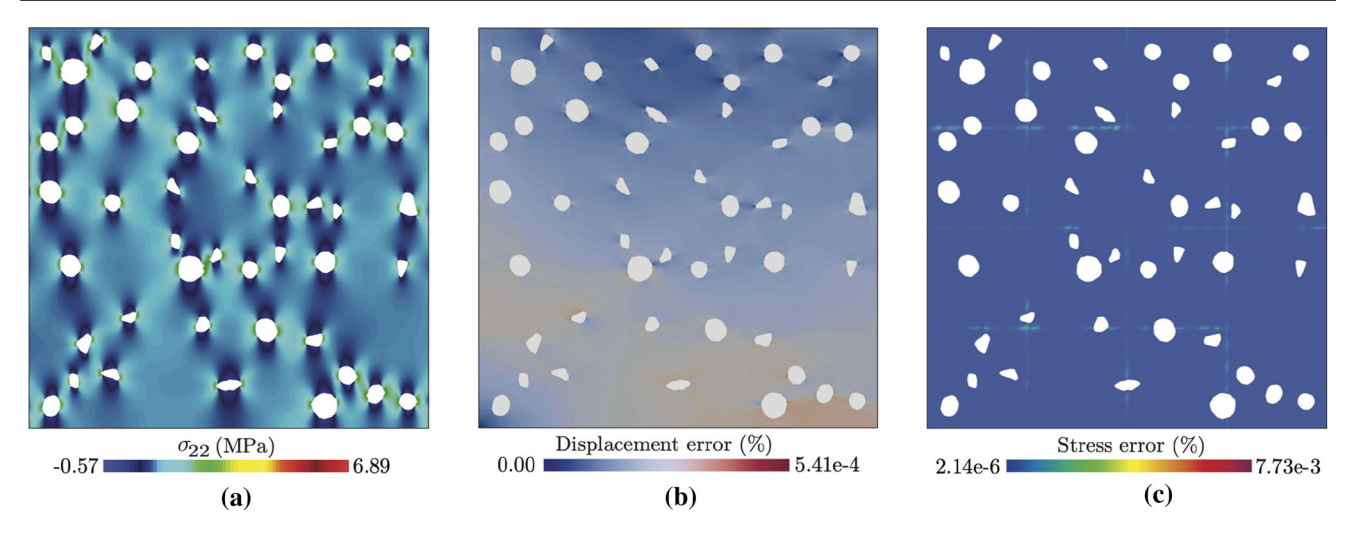


Fig. 10 First example problem: non-overlapping Schwarz approximation of **a** normal stress field in the test problem, together with corresponding distribution of **b** displacement error and **c** stress error using 16 subdomains for partitioning the domain

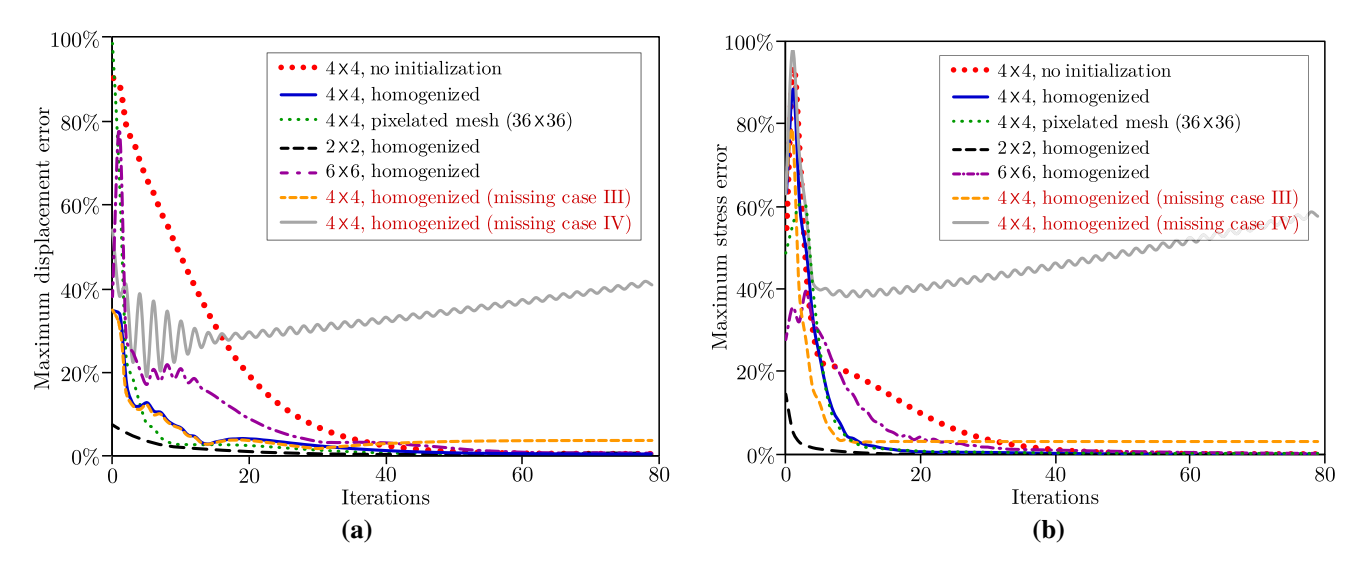


Fig. 11 First example problem: evolution of a maximum displacement error and b maximum stress error in the non-overlapping Schwarz simulation for different model parameters and initialization schemes

model with homogenized properties). As expected, increasing the number of subdomains slows down the convergence, although the 6×6 model with proper initialization of BCs still yields faster convergence than the 4×4 model with no initialization.

To elucidate the importance of proper updating of nodal forces during the FPI process, we have set up two 4×4 partitioned models (homogenized initialization, $\beta = 0.15$) where nodal forces are deliberately updated incorrectly for (i) Case III in Fig. 5b, where external forces are equally distributed between subdomain corner nodes on the top edge of the domain; and (ii) Case IV in Fig. 5c, where required consideration needed for updating BCs at non-matching nodes along subdomain interfaces is overlooked. As shown in Fig. 11, both cases fail to converge due to improperly updating sub-

domain BCs at only a handful of nodes (one node for Case III and three nodes for Case IV). Figure 12 shows the distribution of displacement and stress errors in the model with incorrect updating of nodal forces for Case III, showing a high error at subdomain corners along the upper edge of the domain. However, note this error does not remain local (along with the upper edge of the domain) and has affected other regions of the domain and in particular nearby subdomain corners (cf. Fig. 12b).

In addition to the non-overlapping DDM simulations presented above, we employed the overlapping Schwarz method to approximate the linear elastic response of the test problem. Figure 13 illustrates the resulting distributions of displacement and normal stress errors in this domain after 126 iterations using a 3×3 partitioning pattern with 50% overlap



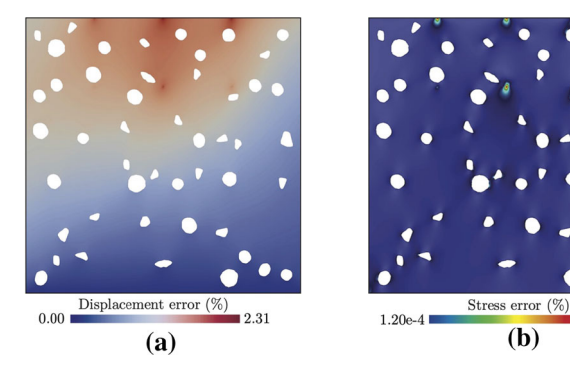


Fig. 12 First example problem: a displacement error and b stress error in the non-overlapping DDM approximation of the linear elastic response in a model partitioned into 16 subdomains with an inappropriate setup for case III while updating nodal forces at subdomain corners along the top edge of the domain

(b)

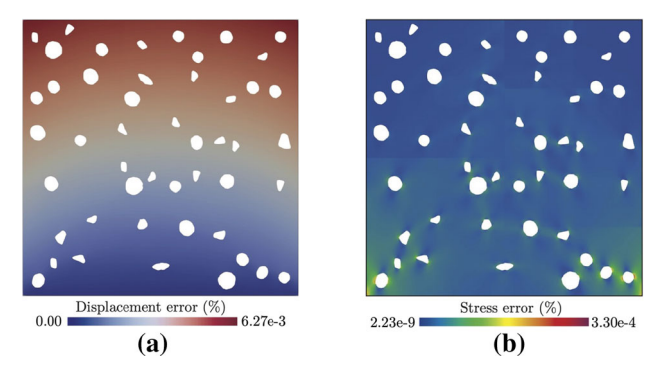


Fig. 13 First example problem: a displacement error and b stress error in the overlapping DDM approximation of the linear elastic response of the test problem using 9 subdomains with 50% overlap

between adjacent subdomains. Similar to non-overlapping simulation results shown in Fig. 10, this simulation yields an excellent accuracy with no concentration of the displacement errors and negligible stress errors along subdomain boundaries. However, the computational cost associated with this overlapping DDM simulation is substantially higher than its non-overlapping counterpart due to both the higher number of iterations and the size of subdomains (50% overlap ratio) associated with the former.

At first glance, it might seem that using a 50% overlap between adjacent subdomains in the DDM simulation above is excessive, as overlapping Schwarz simulations presented in the literature are often conducted with a much less overlap percentage (< 10%). While it is well known that increasing overlapping area between subdomains expedites the DDM convergence, it is worthwhile to study the impact of this parameter on the overall computational cost for modeling the test problem. Figure 14 shows the results of a study on the total number of iterations and computational cost for DDM simulations using 3×3 and 6×6 partitioning patterns with different subdomain overlap percentages. The computational cost values reported in this figure are normalized by the maximum simulation time, which corresponds to the 6 × 6 partitioned domain with 6% overlap between adjacent subdomains. The convergence criterion for all simulations is that the maximum displacement error becomes less than 0.1% in all subdomains. The fact that increasing the number of subdomains increases the number of iterations and therefore the simulation time is a rather trivial outcome. However, note that for the same number of subdomains, using a higher overlap percentage exponentially reduces the computational cost, suggesting that although the larger size of each subdomain increases the cost of simulating its response, the lower number of iterations significantly reduces the total simulation time.

5.1.2 Elastoplastic response

In this section, we implement both the non-overlapping and overlapping Schwarz methods to simulate the elastoplastic response of the test problem. The material properties considered for the porous domain include elastic modulus E=200N m⁻², Poisson's ratio $\nu = 0.1$, yield stress $\sigma_{\rm Y} = 2$ N m⁻², and tangent modulus $E_t = 20 \text{ Nm}^{-2}$. Also, it is assumed that the tensile traction applied along the upper edge of the domain linearly ramps up from 0 to $\bar{t} = 2.5 \text{ N m}^{-1}$ in 20 load steps.

Using the non-overlapping Schwarz approximation for this simulation with 16 partitions (4 \times 4 pattern) and $\beta = 0.1$, it was observed that the FPI solver cannot converge at load step 6. As shown in Fig. 15a, this behavior is due to a high concentration of error at the intersection of one of the voids with the interface between subdomains (3) and (7). Note that although the magnitude of the error at this node is small (but higher than the convergence threshold), accepting this result as a converged solution and moving to the next load step leads to the blowup of the field after a few iterations. The emergence of high errors at this point is attributed to the initiation of plastic deformations in nearby elements of one of the subdomains, while nearby elements of the other subdomain maintain a linear elastic behavior during an FPI iteration. This results in a ping-pong effect while updating nodal force BCs in the vicinity of this point, with the error fluctuating and regions with linear elastic and elastoplastic behavior alternating between the two subdomains without a path towards convergence.

To resolve the convergence issue outlined above, we studied various techniques such as changing the domain partitioning pattern, refining the FE mesh generated for each subdomain, and changing the DDM model parameters. For the current partitioning pattern, further refining the mesh near the problematic void intersecting with (3) and (7) interface or increasing the number of (global) load step was ineffective in resolving the convergence problem. Similarly, using other partitioning patterns $(2 \times 2, 3 \times 3, \text{ etc.})$ led to a similar conver-



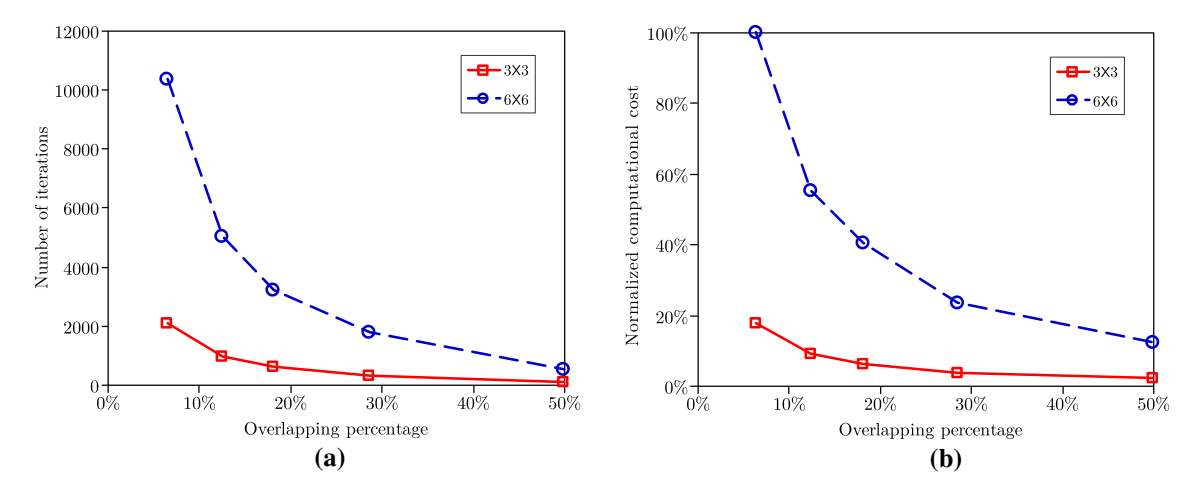
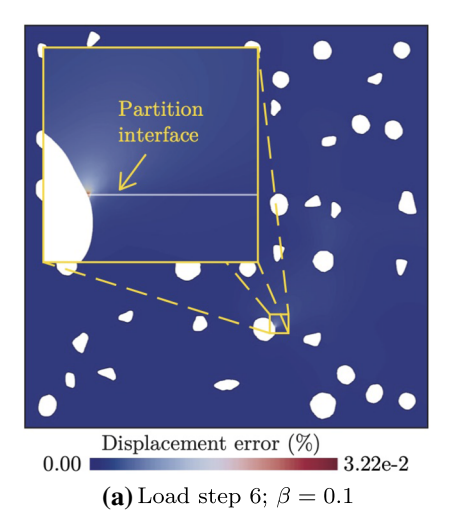
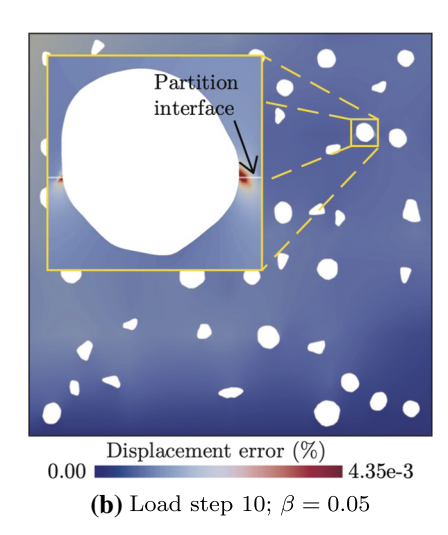


Fig. 14 First example problem: comparison between variations of a number of iterations and b overall computational cost of overlapping Schwarz simulation versus the overlapping percentage of subdomains for 3×3 and 6×6 partitioning patterns

Fig. 15 First example problem: convergence issues in the non-overlapping Schwarz approximation of the elastoplastic response of the test problem reflected in the displacement error at two different load steps and with different β values (4 × 4 partitioning pattern)





gence difficulty at the intersection point of one of the voids with a subdomain interface during the simulation. For the original 4×4 partitioning pattern, the only adjustment that was able to resolve the problem at load step 6 was reducing β to 0.05. However, even this optimistic outcome was shortlived, as a similar issue prohibited the DDM convergence at load step 10 at a different location. As shown in 15b, a similar pattern of high errors emerges near the void intersecting (12) and (16) interface in this simulation. Further reduction of β was not able to resolve this convergence issue, although even if it was feasible the computational cost associated with that would have been exceedingly high. It is worth emphasizing that given the complexity of heterogenous material microstructures, it would practically be impossible to partition the domain such that there is no intersection between embedded heterogeneities and subdomain interfaces.

Unlike the non-overlapping DDM solver, the overlapping Schwarz method could accurately approximate the elastoplastic response of the test problem, regardless of the number of subdomains or their overlap percentage. Figure 16a illustrates the plastic strain field in this porous domain at load step 20, which is simulated using 9 overlapping subdomains $(3 \times 3 \text{ pattern})$ with 50% overlap. The number of DDM iterations associated with the first load step was 147, which was exponentially reduced to less than 30 iterations in the last few load steps. This significant reduction in the number of iterations and consequently the overall computational cost is attributed to the appropriate initialization of Dirichlet BCs along subdomain edges at each load step using (36), which incorporate the information from solutions approximated in previous load steps. Figure 16b, c show distributions of the error in predicting the displacement and plastic strain fields compared to the DNS result, indicating an excellent accuracy and no accumulation of error along with subdomain interfaces.



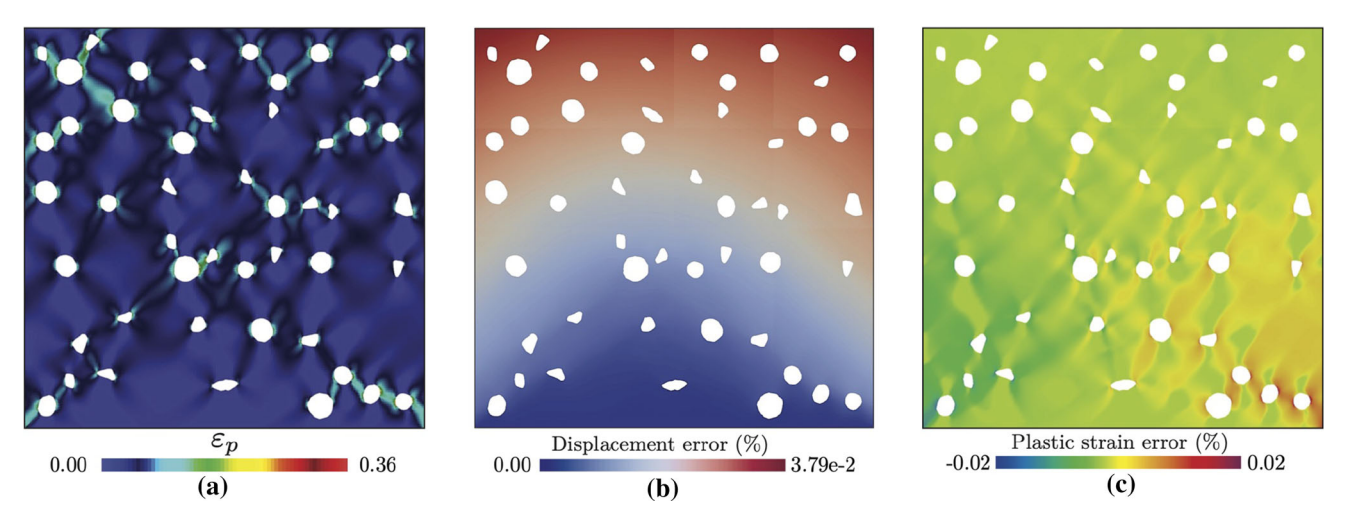


Fig. 16 First example problem: overlapping Schwarz approximation of the elastoplastic response of the test problem. a plastic strain field; b displacement error; c plastic strain error

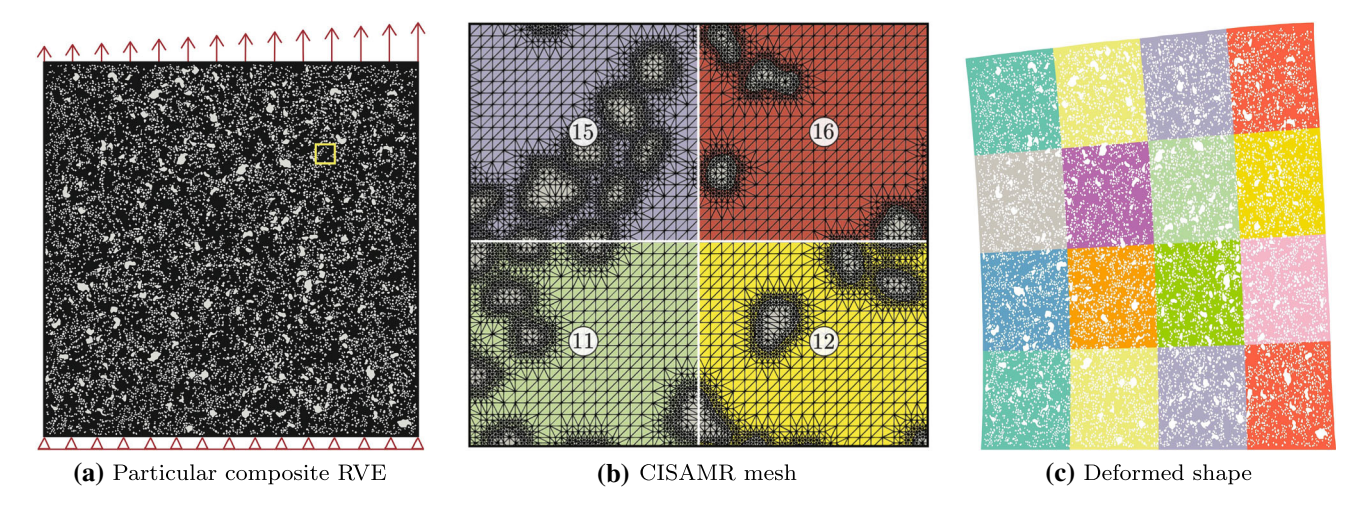


Fig. 17 Second example problem: **a** domain geometry and boundary conditions; **b** small portions of CISAMR meshes at the junction of four subdomains, corresponding to the inset in figure a; **c** non-overlapping

Schwarz simulation of deformed shape of the domain, also showing the 16 subdomains used for partitioning the domain

5.2 Particulate composite

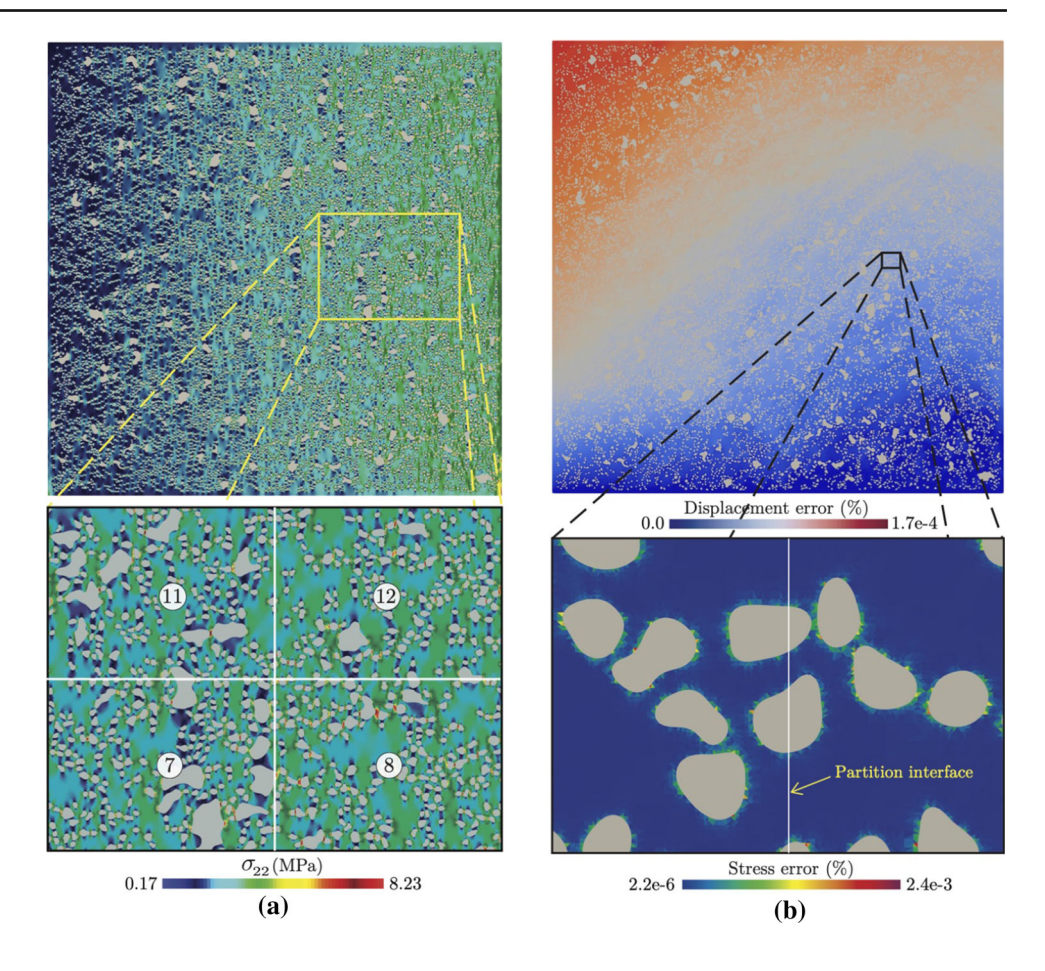
In this example, we show the application of DDM techniques for simulating the linear elastic response of the $800\,\mu\text{m} \times 800\,\mu\text{m}$ particulate composite RVE depicted in Fig. 17a. Elastic properties of the matrix are $E_m=200$ MPa and $v_m=0.1$, while those of more compliant embedded inclusions are $E_p=50$ MPa and $v_p=0.3$. Applied BCs along RVE edges are shown in Fig. 17a, which consist of a fixed displacement BC along the bottom edge and a linear traction along the top edge with minimum and maximum values of $t_{\min}=1~\text{N}\,\text{m}^{-1}$ and $t_{\min}=2~\text{N}\,\text{m}^{-1}$, respectively.

The non-overlapping Schwarz approximation of the field in this RVE is conducted using a 4×4 structured pattern. The CISAMR conforming mesh for each partition is gener-

ated using a 400×400 background mesh with two levels of h-adaptive refinement along with particle-matrix interfaces, resulting in a total number of 7.48 million elements for the entire domain. A small portion of the resulting FE mesh at the junction of four subdomains is depicted in Fig. 17b. To initialize subdomain BCs in the DDM simulation, a 40×40 pixelated mesh with effective elastic moduli ranging from $E_{\rm eff} = 90.73$ MPa to 200 MPa evaluated using (30) for each element was employed to obtain an initial estimate of the field. The DDM simulation was performed using $\beta = 0.15$ and the resulting deformed shape of the domain after 100 iterations is illustrated in Fig. 17c. Also, Fig. 18a shows the resulting stress field, where the inset clearly shows the continuity of stresses across subdomain interfaces/corners. Figure 18b illustrates the distribution of nodal displacement



Fig. 18 Second example problem: non-overlapping Schwarz approximation of a stress field and b resulting displacement/stress errors compared to DNS results using 16 subdomains for partitioning the domain ($\beta = 0.15$)



errors evaluated by comparing the DDM simulation with parallel DNS results, showing an excellent accurate and no accumulation of error along with subdomain interfaces. The inset of Fig. 18b shows a small portion of the domain with the highest stress error, which also has a negligible value.

We also used the overlapping Schwarz method to approximate the linear elastic response of the composite RVE shown in Fig. 17a. 49 partitions (7×7 partitioning pattern) with 50% overlap were used to build the DDM model for this simulation, meaning the subdomain size is similar to that used in the overlapping Schwarz model with only 16 partitions. After 939 iterations, the resulting distributions of displacement and stress errors are depicted in Fig. 19, showing an excellent accuracy in approximating both fields compared to DNS results. However, note that with nearly 3 times more number of subdomains and a much higher number of iterations, this overlapping Schwarz simulation is significantly more computationally demanding than its non-overlapping counterpart. Also, as shown in the previous example, while we could use an overlap ratio of 20% or even 10% to reduce the mesh size for each subdomain, this will disproportionally increase the number of iterations needed for convergence that results in a higher overall computational cost.

Given that the non-overlapping Schwarz method can easily converge without using an excessively small β for predicting the linear elastic response of this RVE and other heterogenous domains we studied, there is no advantage in using the overlapping Schwarz method for modeling such problems. As shown previously, this is not the case for elastoplastic problems, where regardless of the problem size/microstructure and the β value, we observed that the non-overlapping Schwarz method often fails to converge at some load steps. On the contrary, as shown in the next example, the overlapping Schwarz method can easily handle such problems due to avoiding the need to recover/update nodal forces along subdomain edges that intersect with embedded heterogeneities.

5.3 Functionally-graded ceramic material

In this example, we implement the overlapping Schwarz method to simulate the elastoplastic response of the $1600 \,\mu m$ × $1600 \,\mu m$ domain of the functionally graded Ti₃SiC₂-SiC ceramic matrix composite shown in Fig. 20. The composite microstructure is virtually reconstructed using the packing algorithm presented in [75], with the volume fraction of particles varying from $V_f = 10\%$ to 30%. Elastic properties of



Fig. 19 Second example problem: a displacement error and b stress error associated with the overlapping Schwarz approximation using 49 subdomains with 50% overlap

Partition

O.0 Displacement error (%)

4.3e-4

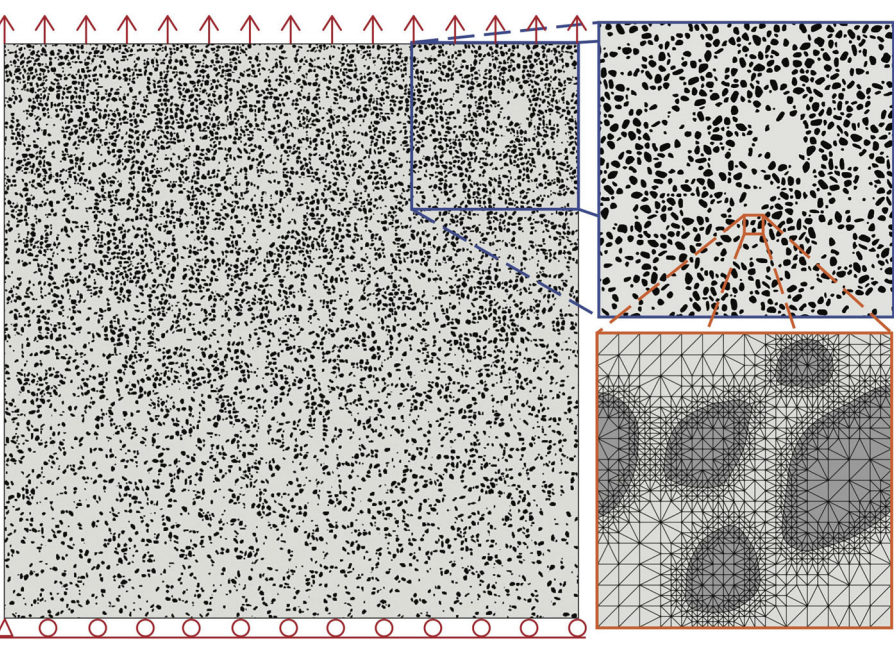
(a)

Stress error (%)

(b)

4.8e-3

Fig. 20 Third example problem: virtually reconstructed domain of a functionally-graded composite. The insets show the arrangement of inclusions in subdomain \mathfrak{F} and a small portion of the conforming mesh generated for this subdomain using CISAMR



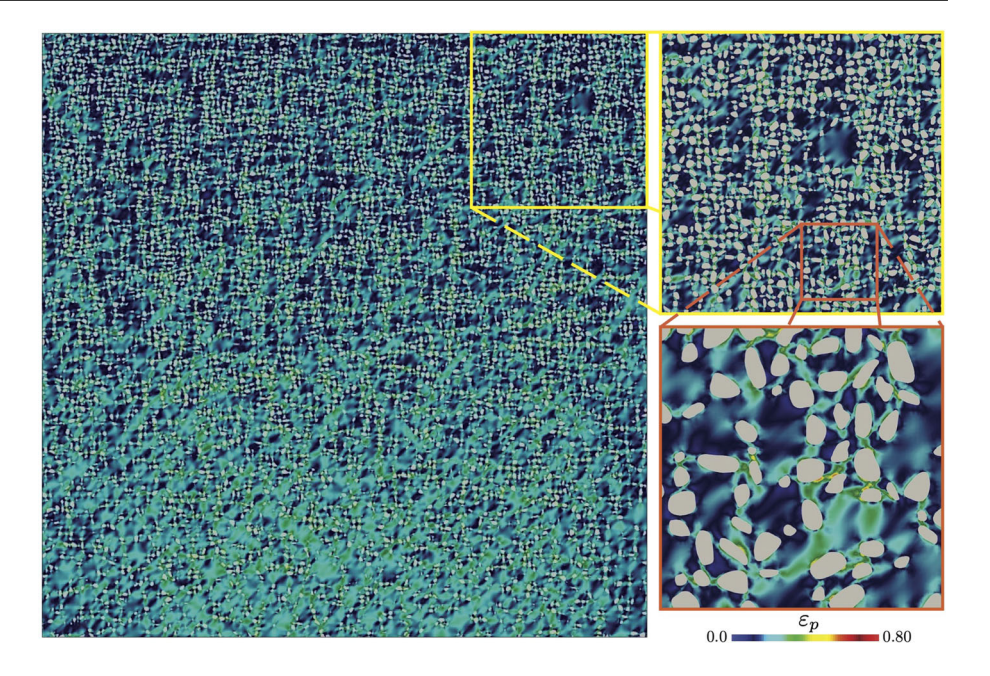
the matrix (Ti₃SiC₂) are $E_m = 326$ GPa and $v_m = 0.19$, while those of embedded inclusions (SiC) are $E_p = 2915$ GPa and $v_p = 0.15$. Further, we have assumed the matrix has an elastoplastic behavior with the yield stress $\sigma_Y = 260$ MPa and tangent modulus $E_t = 8$ GPa. Applied BCs along RVE edges are shown in Fig. 20, which consist of a fixed left-bottom corner, zero displacement in the y-direction along the bottom edge, and a displacement BC applied in the y-direction along the top edge linearly ramping up from 0 to 0.24 N m⁻¹ in 80 load steps.

The overlapping DDM approximation of the field in this RVE is conducted using 36 subdomains (6 \times 6 structured pattern) with 50% overlap. The CISAMR mesh for each subdomain is generated using an 805 \times 805 background mesh with two levels of h-adaptive refinement along with particlematrix interfaces. The total number of elements in the meshes

generated for all 36 subdomains is 6.73 million. The insets of Fig. 20 show the microstructure of subdomain 36, as well as a small portion of the conforming mesh generated for this subdomain. Dirichlet BCs of subdomains in this simulation were initiated using an FE approximation of the field in a 100×100 pixelated mesh with effective properties calculated for each element. Figure 21 shows the resulting plastic strain field at load step 80 after only 3 DDM iterations, while the first load step requires 271 iterations. Note that, as the simulation proceeds, the number of iterations needed for the DDM convergence exponentially reduces at each load step due to the initialization of subdomain BCs from previous steps results. Therefore, despite the high computational cost associated with the first load step, this feature significantly reduces the overall cost and enables performing such a massive nonlinear simulation sequentially using an implicit solver. It is also



Fig. 21 Third example problem: overlapping Schwarz approximation of the plastic strain field in the functionally-graded composite domain after 80 load steps (36 subdomains, 50% overlap)



worth mentioning that due to negligible nonlinear behavior in the first load step, one can implement the non-overlapping Schwarz method at this step and then switch to the overlapping algorithm to further reduce the computational burden.

6 Conclusion

The performance of multi-subdomain DDM techniques was explored for simulating the linear elastic and elastoplastic responses of materials with complex heterogenous microstructures. Both the overlapping and non-overlapping Schwarz methods were reviewed, as the goal is to establish a black-box solver capable of integrating with any commercial FE software that only uses nodal forces and displacements along subdomain boundaries as input/output parameters. Implementations of both methods presented in this manuscript are tightly integrated with the CISAMR meshing algorithm for generating the FE model for each subdomain independently. Several implementation issues of the non-overlapping Schwarz method for modeling heterogenous domains were discussed, including updating BCs, initialization schemes, and FPI acceleration techniques. It was shown that this method can accurately approximate the linear elastic response of composites with complex microstructures at a significantly lower computational cost than the overlapping Schwarz method.

Due to multiple sites of stress concentrations at intersection points of embedded heterogeneities and subdomain interface, the non-overlapping Schwarz method may not achieve convergence when approximating the elastoplastic response of heterogenous materials. On the other hand, regardless of the complexity of the microstructure, the overlapping Schwarz method was able to simulate the elastoplastic response of heterogenous materials at a reasonable computational cost. It was shown that increasing the overlapping percentage between adjacent subdomains for such simulations could exponentially decrease the overall computational cost, which justifies using a high overlap percentage of 50% to achieve a good performance. However, the cost of an overlapping Schwarz method is still higher than its nonoverlapping counterpart, meaning a hybrid approach could potentially yield the best performance for modeling nonlinear problems. In this approach, the latter method can be used in each time step to move toward the final solution and if convergence issues were encountered in some cases, we switch to the former to overcome these issues. Another key advantage of using DDM for simulating the nonlinear response of massive heterogenous domains is the ability to implement an implicit solver for approximating the elastoplastic response of subdomains, while DNS of such problems often requires using an explicit solver to achieve convergence.

Acknowledgements This work has been supported by the Computational Mathematics program of the Air Force Office of Scientific Research (AFOSR) under award number FA9550-21-1-0245 (program officer: Dr. Fariba Fahroo). The authors also acknowledge the allocation of computing time from the Ohio Supercomputer Center (OSC) and the Ohio State University Simulation Innovation and Modeling Center (SIMCenter).



References

- Jäger I, Fratzl P (2000) Mineralized collagen fibrils: a mechanical model with a staggered arrangement of mineral particles. Biophys J 79(4):1737–1746
- Pai S, Kwon J, Liang B et al (2021) Finite element analysis of the impact of bone nanostructure on its piezoelectric response. Biomech Model Mechanobiol. https://doi.org/10.1007/s10237-021-01470-4
- Ahmadian H, Yang M, Soghrati S (2020) Effect of resin-rich zones on the failure response of carbon fiber reinforced polymers. Int J Solids Struct 188–189:74–87
- Kannan R, Hendry S, Higham NJ, Tisseur F (2014) Detecting the causes of ill-conditioning in structural finite element models. Comput Struct 133:79–89
- Yang M, Ji M, Taghipour E, Soghrati S (2018) Cross-linked fiberglass packs: microstructure reconstruction and finite element analysis of the micromechanical behavior. Comput Struct 209:182– 196
- Yang M, Garrard J, Abedi R, Soghrati S (2021) Effect of microstructural variations on the failure response of a nanoenhanced polymer: a homogenization-based statistical analysis. Comput Mech 67(1):315–340
- Baniassadi M, Mortazavi B, Hamedani HA, Garmestani H, Ahzi S, Fathi-Torbaghan M, Ruch D, Khaleel M (2012) Three-dimensional reconstruction and homogenization of heterogeneous materials using statistical correlation functions and FEM. Comput Mater Sci 51(1):372–379
- Rémond Y, Ahzi S, Baniassadi M, Garmestani H (2016) Applied RVE reconstruction and homogenization of heterogeneous materials. Wiley Online Library, Hoboken
- Terada K, Kikuchi N (2001) A class of general algorithms for multi-scale analyses of heterogeneous media. Comput Methods Appl Mech Eng 190(40):5427–5464
- Kanouté P, Boso DP, Chaboche JL, Schrefler B (2009) Multiscale methods for composites: a review. Arch Comput Methods Eng 16(1):31–75
- Inglis HM, Geubelle PH, Matouš K (2008) Boundary condition effects on multiscale analysis of damage localization. Philos Mag 88(16):2373–2397
- Nguyen VP, Stroeven M, Sluys LJ (2011) Multiscale continuous and discontinuous modeling of heterogeneous materials: a review on recent developments. J Multiscale Model 3(04):229–270
- Bahmani B, Yang M, Nagarajan A, Clarke PL, Soghrati S, Abedi R (2019) Automated homogenization-based fracture analysis: effects of SVE size and boundary condition. Comput Methods Appl Mech Eng 345:701–727
- Feyel F (1999) Multiscale FE² elastoviscoplastic analysis of composite structures. Comput Mater Sci 16(1):344–354
- Li C, Chou T-W (2006) Multiscale modeling of compressive behavior of carbon nanotube/polymer composites. Compos Sci Technol 66(14):2409–2414
- Totry E, González C, LLorca J (2008) Prediction of the failure locus of c/peek composites under transverse compression and longitudinal shear through computational micromechanics. Compos Sci Technol 68(15):3128–3136
- Feyel F (2003) A multilevel finite element method (FE²) to describe the response of highly non-linear structures using generalized continua. Comput Methods Appl Mech Eng 192(28):3233–3244
- Ahmadian H, Yang M, Nagarajan A, Soghrati S (2019) Effects of shape and misalignment of fibers on the failure response of carbon fiber reinforced polymers. Comput Mech 63(5):999–1017
- Liang B, Nagarajan A, Ahmadian H, Soghrati S (2019) Analyzing effects of surface roughness, voids, and particle-matrix interfacial

- bonding on the failure response of a heterogeneous adhesive. Comput Methods Appl Mech Eng 346:410–439
- Dvorak GJ (1992) Transformation field analysis of inelastic composite materials. Proc R Soc Lond A 437(1900):311–327
- Michel J-C, Suquet P (2004) Computational analysis of nonlinear composite structures using the nonuniform transformation field analysis. Comput Methods Appl Mech Eng 193(48–51):5477– 5502
- Amsallem D, Farhat C (2008) Interpolation method for adapting reduced-order models and application to aeroelasticity. AIAA J 46(7):1803–1813
- Liu Z, Bessa M, Liu WK (2016) Self-consistent clustering analysis: an efficient multi-scale scheme for inelastic heterogeneous materials. Comput Methods Appl Mech Eng 306:319–341
- Gao J, Shakoor M, Domel G, Merzkirch M, Zhou G, Zeng D, Su X, Liu WK (2020) Predictive multiscale modeling for unidirectional carbon fiber reinforced polymers. Compos Sci Technol 186:107922
- 25. Balay S, Abhyankar S, Adams M, Brown J, Brune P, Buschelman K, Dalcin L, Dener A, Eijkhout V, Gropp W, Karpeyev D, Kaushik D, Knepley M, May D, Curfman McInnes L, Mills R, Munson T, Rupp K, Sanan P, Smith B, Zampini S, Zhang H, Zhang H (2021) PETSc users manual. Technical report ANL-95/11 Revision 3.15, Argonne National Laboratory
- Gosselet P, Rey C (2006) Non-overlapping domain decomposition methods in structural mechanics. Arch Comput Methods Eng 13(4):515–572
- Li J, Hon YC (2004) Domain decomposition for radial basis meshless methods. Numer Methods Partial Differ Equ 20(3):450–462
- Fragakis Y, Papadrakakis M (2003) The mosaic of high performance domain decomposition methods for structural mechanics: formulation, interrelation and numerical efficiency of primal and dual methods. Comput Methods Appl Mech Eng 192(35–36):3799–3830
- Cai X (2003) Overlapping Domain Decomposition Methods. In: Langtangen HP, Tveito A (eds) Advanced Topics in Computational Partial Differential Equations. Lecture Notes in Computational Science and Engineering, vol 33. Springer, Berlin, Heidelberg. https://doi.org/10.1007/978-3-642-18237-2_2
- Chan TF, Mathew TP (1994) Domain decomposition algorithms.
 Acta Numer 3(1):61–143
- Smith B, Bjorstad P, Gropp W (2004) Domain decomposition: parallel multilevel methods for elliptic partial differential equations. Cambridge University Press, Cambridge
- Elleithy WM, Al-Gahtani HJ (2000) An overlapping domain decomposition approach for coupling the finite and boundary element methods. Eng Anal Bound Elem 24(5):391–398
- Zhou X, Hon YC, Li J (2003) Overlapping domain decomposition method by radial basis functions. Appl Numer Math 44(1–2):241– 255
- Elleithy WM, Tanaka M (2003) Interface relaxation algorithms for BEM-BEM coupling and FEM-BEM coupling. Comput Methods Appl Mech Eng 192(26–27):2977–2992
- Quarteroni A, Valli A (1999) Domain decomposition methods for partial differential equations. Oxford University Press, Oxford
- Le Tallec P (1994) Domain decomposition methods in computational mechanics. Comput Mech Adv 1(2):121–220
- Farhat C, Roux F-X (1991) A method of finite element tearing and interconnecting and its parallel solution algorithm. Int J Numer Methods Eng 32(6):1205–1227
- Tallec P, Roeck Y, Vidrascu M (1991) Domain decomposition methods for large linearly elliptic three-dimensional problems. J Comput Appl Math 34(1):93–117
- Farhat C, Mandel J, Roux FX (1994) Optimal convergence properties of the FETI domain decomposition method. Comput Methods Appl Mech Eng 115(3–4):365–385



- Mandel J (1993) Balancing domain decomposition. Commun Numer Methods Eng 9(3):233–241
- Farhat C, Lesoinne M, Pierson K (2000) A scalable dual-primal domain decomposition method. Numer Linear Algebra Appl 7(7– 8):687–714
- Farhat C, Lesoinne M, LeTallec P, Pierson K, Rixen D (2001) FETI-DP: a dual-primal unified FETI method-part I: a faster alternative to the two-level FETI method. Int J Numer Methods Eng 50(7):1523– 1544
- Klawonn A, Widlund OB (2006) Dual-primal FETI methods for linear elasticity. Commun Pure Appl Math A J Issued Courant Inst Math Sci 59(11):1523–1572
- Klawonn A, Rheinbach O (2007) Robust FETI-DP methods for heterogeneous three dimensional elasticity problems. Comput Methods Appl Mech Eng 196(8):1400–1414
- Mandel J, Dohrmann CR (2003) Convergence of a balancing domain decomposition by constraints and energy minimization. Numer Linear Algebra Appl 10(7):639–659
- Mandel J, Dohrmann CR, Tezaur R (2005) An algebraic theory for primal and dual substructuring methods by constraints. Appl Numer Math 54(2):167–193
- Klawonn A, Lanser M, Rheinbach O (2014) Nonlinear FETI-DP and BDDC methods. SIAM J Sci Comput 36(2):A737–A765
- Klawonn A, Lanser M, Rheinbach O, Uran M (2017) Nonlinear FETI-DP and BDDC methods: a unified framework and parallel results. SIAM J Sci Comput 39(6):C417–C451
- Papadrakakis M, Stavroulakis G, Karatarakis A (2011) A new era in scientific computing: domain decomposition methods in hybrid CPU–GPU architectures. Comput Methods Appl Mech Eng 200(13–16):1490–1508
- Gendre L, Allix O, Gosselet P, Comte F (2009) Non-intrusive and exact global/local techniques for structural problems with local plasticity. Comput Mech 44(2):233–245
- Duval M, Passieux JC, Salaün M, Guinard S (2016) Non-intrusive coupling: recent advances and scalable nonlinear domain decomposition. Arch Comput Methods Eng 23(1):17–38
- Gosselet P, Blanchard M, Allix O et al (2018) Non-invasive globallocal coupling as a Schwarz domain decomposition method: acceleration and generalization. Adv Model Simul Eng Sci 5:4. https://doi.org/10.1186/s40323-018-0097-4
- Kim NH (2014) Introduction to nonlinear finite element analysis.
 Springer, Berlin
- Kim NH, Choi KK, Chen JS (2000) Shape design sensitivity analysis and optimization of spatially rotating objects. AIAA J 38(9):1742–1753
- 55. Bleyer J (2018) Numerical Tours of Computational Mechanics with FEniCS. Zenodo. https://doi.org/10.5281/zenodo.1287832
- Simo JC, Taylor RL (1985) Consistent tangent operators for rateindependent elastoplasticity. Comput Methods Appl Mech Eng 48(1):101–118
- de Boer A, van Zuijlen AH, Bijl H (2007) Review of coupling methods for non-matching meshes. Comput Methods Appl Mech Eng 196(8):1515–1525
- Soghrati S, Nagarajan A, Liang B (2017) Conforming to Interface structured adaptive mesh refinement technique for modeling heterogeneous materials. Comput Mech 125:24–40
- Nagarajan A, Soghrati S (2018) Conforming to interface structured adaptive mesh refinement: 3d algorithm and implementation. Comput Mech 62(5):1213–1238
- Liang B, Nagarajan A, Soghrati S (2019) Scalable parallel implementation of cisamr: a non-iterative mesh generation algorithm. Comput Mech 64(1):173–195

- Miled K, Sab K, Le Roy R (2011) Effective elastic properties of porous materials: homogenization schemes vs experimental data. Mech Res Commun 38(2):131–135
- 62. Küttler U, Wall WA (2008) Fixed-point fluid-structure interaction solvers with dynamic relaxation. Comput Mech 43(1):61–72
- Küttler U, Wall WA (2009) Vector extrapolation for strong coupling fluid–structure interaction solvers. J Appl Mech Trans ASME 76(2):1–7
- Smith DA, Ford WF, Sidi A (1987) Extrapolation methods for vector sequences. SIAM Rev 29(2):199–233
- Sidi A (1991) Efficient implementation of minimal polynomial and reduced rank extrapolation methods. J Comput Appl Math 36(3):305–337
- Jbilou K, Sadok H (1999) LU implementation of the modified minimal polynomial extrapolation method for solving linear and nonlinear systems. IMA J Numer Anal 19(4):549–561
- 67. Uekermann B, Bungartz HJ, Gatzhammer B, Mehl M (2013) A parallel, black-box coupling algorithm for fluid–structure interaction. In: COUPLED PROBLEMS 2013—Proceedings of the 5th international conference on coupled problems in science and engineering, pp 241–252
- 68. Lindner F, Mehl M, Scheufele K, Uekermann B (2015) A comparison of various quasi-Newton schemes for partitioned fluid–structure interaction. In: COUPLED PROBLEMS 2015—Proceedings of the 6th international conference on coupled problems in science and engineering, pp 477–488
- Bogaers AE, Kok S, Reddy BD, Franz T (2014) Quasi-Newton methods for implicit black-box FSI coupling. Comput Methods Appl Mech Eng 279:113–132
- Bungartz HJ, Lindner F, Mehl M, Uekermann B (2015) A plugand-play coupling approach for parallel multi-field simulations. Comput Mech 55(6):1119–1129
- Bungartz HJ, Lindner F, Gatzhammer B, Mehl M, Scheufele K, Shukaev A, Uekermann B (2016) preCICE—a fully parallel library for multi-physics surface coupling. Comput Fluids 141:250–258
- Mehl M, Uekermann B, Bijl H, Blom D, Gatzhammer B, Van Zuijlen A (2016) Parallel coupling numerics for partitioned fluid– structure interaction simulations. Comput Math Appl 71(4):869– 891
- Spenke T, Hosters N, Behr M (2020) A multi-vector interface quasi-Newton method with linear complexity for partitioned fluid-structure interaction. Comput Methods Appl Mech Eng 361:112810
- Mota A, Tezaur I, Alleman C (2017) The Schwarz alternating method in solid mechanics. Comput Methods Appl Mech Eng 319:19–51
- Yang M, Nagarajan A, Liang B, Soghrati S (2018) New algorithms for virtual reconstruction of heterogeneous microstructures. Comput Methods Appl Mech Eng 338:275–298

Publisher's Note Springer Nature remains neutral with regard to jurisdictional claims in published maps and institutional affiliations.

